J Neurophysiol 122: 151–175, 2019.
First published May 1, 2019; doi:10.1152/jn.00029.2019.

RESEARCH ARTICLE | *Cellular and Molecular Properties of Neurons*

Response to coincident inputs in electrically coupled primary afferents is heterogeneous and is enhanced by H-current (IH) modulation

Federico Davoine[1] and Sebastian Curti[2]

[1]*Instituto de Física e Instituto de Ingeniería Eléctrica, Facultad de Ingeniería, Universidad de la República, Montevideo, Uruguay; and* [2]*Laboratorio de Neurofisiología Celular, Departamento de Fisiología, Facultad de Medicina, Universidad de la República, Montevideo, Uruguay*

Submitted 15 January 2019; accepted in final form 22 April 2019

Davoine F, Curti S. Response to coincident inputs in electrically coupled primary afferents is heterogeneous and is enhanced by H-current (IH) modulation. *J Neurophysiol* 122: 151–175, 2019. First published May 1, 2019; doi:10.1152/jn.00029.2019.—Electrical synapses represent a widespread modality of interneuronal communication in the mammalian brain. These contacts, by lowering the effectiveness of random or temporally uncorrelated inputs, endow circuits of coupled neurons with the ability to selectively respond to simultaneous depolarizations. This mechanism may support coincidence detection, a property involved in sensory perception, organization of motor outputs, and improvement signal-to-noise ratio. While the role of electrical coupling is well established, little is known about the contribution of the cellular excitability and its modulations to the susceptibility of groups of neurons to coincident inputs. Here, we obtained dual whole cell patch-clamp recordings of pairs of mesencephalic trigeminal (MesV) neurons in brainstem slices from rats to evaluate coincidence detection and its determinants. MesV neurons are primary afferents involved in the organization of orofacial behaviors whose cell bodies are electrically coupled mainly in pairs through soma-somatic gap junctions. We found that coincidence detection is highly heterogeneous across the population of coupled neurons. Furthermore, combined electrophysiological and modeling approaches reveal that this heterogeneity arises from the diversity of MesV neuron intrinsic excitability. Consistently, increasing these cells' excitability by upregulating the hyperpolarization-activated cationic current (I_H) triggered by cGMP results in a dramatic enhancement of the susceptibility of coupled neurons to coincident inputs. In conclusion, the ability of coupled neurons to detect coincident inputs is critically shaped by their intrinsic electrophysiological properties, emphasizing the relevance of neuronal excitability for the many functional operations supported by electrical transmission in mammals.

NEW & NOTEWORTHY We show that the susceptibility of pairs of coupled mesencephalic trigeminal (MesV) neurons to coincident inputs is highly heterogenous and depends on the interaction between electrical coupling and neuronal excitability. Additionally, upregulating the hyperpolarization-activated cationic current (I_H) by cGMP results in a dramatic increase of this susceptibility. The I_H and electrical synapses have been shown to coexist in many neuronal populations, suggesting that modulation of this conductance could represent a common strategy to regulate circuit operation supported by electrical coupling.

electrical synapses; HCN channels; mesencephalic trigeminal neurons

INTRODUCTION

Electrical transmission through gap junctions is typically fast and bidirectional, supporting the synchronized activation of networks of coupled neurons (Bennett and Zukin 2004; Connors and Long 2004; Perez Velazquez and Carlen 2000). Also, these contacts may endow neural circuits with the ability to selectively respond to excitatory synchronic inputs (Curti et al. 2012; Galarreta and Hestrin 2001; Veruki and Hartveit 2002a). In fact, if a cell of a network of coupled neurons receives a synaptic input, part of the underlying current flows through gap junctions toward nonstimulated cells. Thereby, by acting as current sinks, electrical synapses reduce the input resistance of all cells of the network. This effect, termed loading, greatly reduces the excitability of electrically coupled neurons (Getting 1974). In contrast, synchronic inputs to all coupled cells promote parallel variations of the membrane potential of each neuron, reducing the voltage drop across junctions and minimizing the flow of current to neighbor cells. Thus, by canceling the loading effect, simultaneous inputs induce larger changes in membrane potential of all neurons of the network, facilitating their activation. This property allows electrical coupling to maximize the impact of coincident inputs while dampening that of temporally dispersed ones, supporting coincidence detection (Chillemi et al. 2007; Edwards et al. 1998; Hjorth et al. 2009; Rabinowitch et al. 2013; Rela and Szczupak 2004). In this way circuits of coupled neurons can discriminate inputs based on their arrival times. Critical for this network operation is the difference of neuronal responses evoked by coincident excitatory inputs compared with randomly distributed ones. The greater the contrast between maximal (due to coincident inputs) and minimal responses (due to temporally dispersed inputs), the higher the gain of coincidence detection. Thus any mechanism that increases this contrast, whether increasing the response to coincident inputs or by reducing it to uncorrelated ones, will enhance coincident detection (Agmon-Snir et al. 1998). While the mechanisms determining the precision of coincidence detection in networks of coupled neurons have been studied (Edwards et al. 1998), much less is known about the mechanisms that support its gain.

The mesencephalic trigeminal (MesV) nucleus of the rat is a particularly good model to study electrical transmission and its contributions to the computational capabilities of neural networks. These neurons are primary afferents, therefore exhibit-

Address for reprint requests and other correspondence: S. Curti, Gral, Flores 2125, Montevideo 11800, Uruguay (e-mail: scurti@fmed.edu.uy).

ing a simple morphology characterized by a large cell body from which only one process emerges. Also, they are electrically coupled in pairs or small clusters through distinct soma-somatic connexin36 (Cx36)-containing gap junctions (Curti et al. 2012). Interestingly, MesV neurons receive profuse synaptic inputs from several brain structures (Lazarov 2002) by way of neurotransmitters and neuromodulators that have been shown to modulate either neuronal excitability or electrical coupling in other systems, raising the possibility of regulatory control.

In a previous study, we showed that electrically coupled MesV neurons act as coincidence detectors (Curti et al. 2012). Beyond the well-established role of electrical coupling in coincidence detection, the present study shows that the intrinsic electrophysiological properties of coupled neurons are also critical determinants of this network operation. Moreover, the susceptibility to coincident inputs, corresponding to the gain of coincidence detection, is highly heterogeneous across the population of coupled cells. Furthermore, by combining electrophysiological and modeling approaches, we provide evidence supporting the notion that this heterogeneity arises to a great extent from the diverse regulatory states of MesV neuron's intrinsic excitability. Consistently, the upregulation of the hyperpolarization-activated cationic current (I_H) triggered by cGMP results in a dramatic enhancement of the susceptibility of coupled MesV neurons to coincident excitatory inputs. Modulatory actions induced by cGMP consist of a shift of the I_H activation curve toward more positive values and an acceleration of its kinetics, resulting in a depolarization of the resting membrane potential, a reduction of the input resistance, and an enhancement in neuronal firing. In coupled neurons, these modulatory changes in combination with the loading effect result in a dramatic increase in firing mainly in response to coincident depolarizations. Thus, by preferentially increasing neuronal excitability to simultaneous inputs, upregulation of I_H causes an enhancement of coincidence detection gain.

These results indicate that modulation of the I_H might impart highly dynamic and relevant characteristics to electrical synaptic transmission. According to that, network operations supported by this modality of intercellular communication are critically shaped by the intrinsic excitability of neurons, emphasizing the relevance of the neuronal electrophysiological properties and its modulations in the many functional operations supported by electrical transmission in the mammalian brain.

MATERIALS AND METHODS

The experimental protocol was approved by the local animal ethics committee of Facultad de Medicina, according to the guidelines of Comisión Honoraria de Experimentación Animal of Universidad de la República (Uruguay), with minimization of the numbers of animals used.

Experimental design. Transverse brain stem slices (250-μm thick) were prepared from Wistar or Sprague-Dawley rats of either sex (age: postnatal *days 8–18*). Rats were decapitated without anesthesia, and brains were quickly removed. Slices obtained using a vibratome (Leica VT 1000s or DSK DTK-1000) were placed in cold sucrose solution containing the following (in mM): 248 sucrose, 2.69 KCl, 1.25 KH_2PO_4, 26 $NaHCO_3$, 10 glucose, 2 $CaCl_2$, and 2 $MgSO_4$ bubbled with 95% O_2-5% CO_2 (pH ~7.4). The slices were then transferred to an incubation chamber filled with sucrose solution at room temperature and kept there for 60 min. The sucrose solution was slowly replaced by physiological solution containing the following (in mM): 124 NaCl, 2.69 KCl, 1.25 KH_2PO_4, 26 $NaHCO_3$, 10 glucose, 2 $CaCl_2$, and 2 $MgSO_4$ bubbled with 95% O_2-5% CO_2 (pH ~7.4). Sections were kept at room temperature in the physiological solution until they were transferred into the recording chamber. The recording chamber, mounted on an upright microscope stage (Nikon Eclipse E600), was continuously perfused with physiological solution (1–1.5 ml/min) at room temperature. Whole cell patch recordings were performed under visual control using infrared differential interference contrast optics. MesV neurons were identified on the basis of their location, large spherical somata, and characteristic electrophysiological properties in response to both depolarizing and hyperpolarizing current pulses (Del Negro and Chandler 1997; Liem et al. 1991; Pedroarena et al. 1999). Recording pipettes pulled from borosilicate glass (4–8 MΩ) were filled with intracellular solution containing the following (in mM): 144 K-gluconate, 3 $MgCl_2$, 0.2 EGTA, 4 Mg-ATP, 0.3 Na-ATP, and 10 HEPES (pH ~7.2). The seal resistance between the electrode tip and the cell membrane was >1 GΩ, and pipette capacitance was compensated before breaking the seal. Simultaneous recordings from pairs of MesV neurons whose cell bodies lie in close apposition were made using one Axopatch 200B and one Axoclamp 2A amplifiers or a Multiclamp 700B amplifier (Molecular Devices, Sunnyvale, CA). Only cells displaying resting membrane potential more negative than -50 mV and spike amplitude above 70 mV were included in this report. Recordings were low-pass-filtered at 5 kHz and acquired by means of an analog to digital converter connected to a computer, sampled at 20 or 10 KHz depending on the experiment. Data were analyzed using Axograph X, pClamp 9 (Molecular Devices) and Igor (Wave Metrics, Portland OR) software.

Calculation of coupling coefficient. During simultaneous intracellular recordings of pairs of MesV neurons in current clamp, hyperpolarizing current pulses of 200–400 ms in duration were alternatively injected to each cell and the resulting membrane voltage deflections were measured in both cells. The coupling coefficient (CC) from a presynaptic to a postsynaptic cell, being the presynaptic cell defined as the one receiving the current injection, was calculated as V_{post}/V_{pre}, where V_{pre} is the voltage deflection in the presynaptic neuron and V_{post} the concomitant voltage deflection in the postsynaptic neuron. A total of 10 to 100 single responses were averaged to improve the signal-to-noise ratio. Because the strength of an electrical synapse measured as the CC is influenced by both the gap junction conductance and the input resistance of the postsynaptic cell (Bennett 1966; Curti and O'Brien 2016), any voltage-dependent change of the input resistance of the postsynaptic cell might modify the CC. Hence, to improve the accuracy of CC estimation, instead of same amplitude current pulses a series of hyperpolarizing current pulses of different amplitudes (-50 to -450 pA) were applied. This method was employed in some cases in which inconsistencies in the CC estimation were observed due to the above-mentioned pitfalls. From these recordings, plots of the voltage change in the postsynaptic neuron as a function of the voltage change in the presynaptic neuron were constructed and CC was estimated from the slope of linear regressions (see Fig. 11, *C* and *D*). For each pair of coupled neurons, the CC was calculated in opposite directions and both values were reported (two directions per coupled pair).

Estimation of gap junction conductance. With the use of the same experimental protocol described in *Calculation of coupling coefficient*, the conductance of electrical contacts was estimated as the reciprocal of the resistance (R_c) calculated following (Bennett 1966):

$$R_c = \frac{Rin_{pre} \times Rin_{post} - R_t^2}{R_t}$$

where Rin_{pre} and Rin_{post} are the input resistance of the pre- and postsynaptic cells, respectively, and R_t is the transfer resistance defined as the voltage response amplitude in the postsynaptic cell

divided by the current intensity injected in the presynaptic cell. Conductance values estimated by this method are reported as directions (2 directions per coupled pair). To assess the accuracy of this method in estimating the gap junction conductance between MesV neurons, in an independent experimental series we compared the results obtained by using this indirect method with those obtained from direct measurements of junctional current under voltage clamping. For that purpose dual voltage-clamp experiments were performed following the same procedure we employed previously for the characterization of electrical transmission in the MesV nucleus (Curti et al. 2012). The results obtained by these two approaches were indistinguishable, averaging 4.0 ± 0.59 and 4.2 ± 0.72 nS (SE) for current- and voltage-clamp experiments, respectively ($P = 0.582$, $n = 8$; paired, two-tailed *t*-test).

Calculation of coincidence detection index. To assess coincidence detection, suprathreshold depolarizing current pulses were applied to pairs of MesV neurons. Pulses, whose intensity were adjusted to evoke only one or two spikes when applied individually, were repeated 10–20 times independently to each cell and then to both cells at the same time. From these recordings, the average number of spikes evoked in each cell during these stimulation protocols was determined. To quantify coincidence detection, two alternative methods were considered. The first one consisted of calculating the ratio of the number of spikes when cells were simultaneously activated over the number of spikes when cells were independently activated. This index will indicate how much stronger is the response to coincident stimulation relative to individual responses. The second method consisted of calculating an index defined as the subtraction of the mean number of spikes when cells were independently activated from the mean number of spikes when cells were simultaneously activated (coincident activation). This index reflects how many spikes are added to the neuronal response when this cell and its coupled neighbor were activated at the same time (when the loading effect is canceled, see text) in comparison to when the cell was activated in isolation. For the whole population of recorded coupled cells ($n = 76$), the two methods yield comparable results as indicated by paired, two-tailed *t*-test ($P = 0.19$) and the fact that they present a clear positive correlation {slope = 0.63 ± 0.036 [95% confidence interval (CI)], $R^2 = 0.8$}. Because difference in firing evoked by simultaneous and uncorrelated inputs is considered a direct indicator of coincidence detection function (Agmon-Snir et al. 1998), the subtraction index (coincidence detection index) was adopted. Thus this index represents a measurement of the susceptibility of coupled neurons to coincident inputs and has units of spikes. Despite coincidence detection in coupled neurons represents an emergent property of groups of cells, we calculated the coincidence detection index based on the activity of single neurons (considering the activity in the stimulated neuron) to be able to correlate this property with their intrinsic excitability.

Assessment of MesV neurons excitability. During current-clamp recordings, series of depolarizing current pulses of 200 ms in duration were applied, whose intensities ranged most typically from 50 to 650 pA, in steps of 50 pA. From these recordings, curves of the number of spikes versus current intensity were constructed and threshold intensity and the number of spikes evoked by current pulses three to six times this intensity were determined. This analysis showed that even at comparable ages healthy neurons display a wide diversity of firing properties in terms of the number of spikes and the threshold intensity. To assess excitability, straight line functions were fitted to spikes versus current curves. Even though in some cases the goodness of fit to these functions was relatively poor (particularly for step like curves), by forcing the fitting through the origin, the slope of this curve represents a valuable indicator of neuronal excitability. In fact, by pivoting around the origin, the slope of this function is a highly sensitive indicator that combines both the ability of the neuron to produce repetitive discharges and the threshold level.

Recording of the persistent Na^+ current. To isolate the persistent Na^+ current (I_{NaP}), K^+ currents were blocked either by using a Cs^+ based intracellular solution (in mM: 123 Cs-glutamate, 9 HEPES, 4.5 EGTA, 0.27 Na-GTP, 3.6 Na_2-ATP, and 9.5 $MgCl_2$, pH ~7.2 and osmolarity adjusted to 295–305 mosM), or by using a normal K^+-based intracellular solution (see above) and adding a combination of blockers to the extracellular solution (5 mM TEA-Cl, 1 mM 4-aminopyridine, and 1 mM CsCl). In both cases, 0.2 mM $CdCl_2$ were added to the extracellular solution to block Ca^{2+} currents. Both methods yield comparable results. MesV neurons were voltage clamped and ramp protocols were applied from a holding potential of −70 to 0 mV in 4 s (Fleidervish and Gutnick 1996). These protocols evoked a slow inward current that peaked at about −40 mV and that was totally abolished by adding 0.5 μM tetrodotoxin to the extracellular solution.

Recording of I_H. In the whole cell configuration, compensation of the cell capacitance and series resistance (80%) was performed and monitored during the course of experiments. Recordings were low-pass filtered at 5 KHz and sampled at 20 KHz. Voltage steps of 0.5 to 2 s in duration and from −40 to −140 mV were applied starting from a holding potential of −50 mV and returning to a postpulse potential of −70 or −80 mV. This protocol was applied in control conditions and in the presence of 2 mM CsCl in the bath, which almost completely blocks the I_H (Pape 1996). To isolate this current from other voltage activated membrane currents, total currents obtained in presence of CsCl were subtracted from those obtained in control conditions. In selected control experiments ($n = 4$), I_H isolation was achieved by using a combination of 0.5 μM tetrodotoxin and 1 mM 4-aminopyridine to block the main voltage-activated currents of MesV neurons at the explored voltage range, that is, the persistent sodium current and the A-type K^+ current, respectively (Del Negro and Chandler 1997; Wu et al. 2001). Membrane currents obtained by these two procedures were undistinguishable; therefore, the CsCl procedure was adopted for simplicity.

Steady-state activation curves were determined from the amplitude of tail currents after voltage steps return to −70 or −80 mV. Tail current amplitudes were measured after the decay of the capacitive transients (typically ~4 ms of terminated the pulse) and transformed to conductance values dividing by the driving force (−41.3 and −51.3 mV, respectively). For this purpose, the reversal potential of the I_H was determined following standard protocols consisting in voltage steps to −110 mV from a holding potential of −50 mV. Voltage steps lasted for 700 ms to 1 s to produce near maximal activation of the I_H and were followed by a series of voltage postpulses that ranged from −10 to −80 mV. Membrane currents were recorded during the postpulses after the decay of the capacitive transient. Measured membrane current values were plotted against the postpulse voltage, and the reversal potential was determined as the point where $I_H = 0$ (intersection with the voltage axis). Following this procedure, the reversal potential was determined in five neurons and averaged −28.7 ± 1.52 mV (SE).

For each cell, the conductance values (G) obtained following this procedure were normalized by its maximum value (G_{max}) and plotted as a function of the step voltages and fitted to a Boltzmann equation of the form:

$$\frac{G}{G_{max}}(V) = \frac{1}{1 + exp\left[\left(V_{1/2} - V\right)/K\right]}$$

where V is the voltage during the command pulse in millivolts, $V_{1/2}$ is the half activation voltage, and K is the slope of the fitting curve at $V_{1/2}$.

For the population of recorded MesV neurons, the series resistance (R_s) averaged 12.4 ± 0.59 MΩ (SE) and was compensated by 80%. The maximum error in voltage-clamp commands introduced by the uncompensated R_s was estimated for each experiment by multiplying the uncompensated series resistance (20% of R_s) times the maximum membrane current at steady state elicited by the most hyperpolarizing command potential. This error averaged 6.2 ± 2.72% (SD, range

2–13%, $n = 34$) of command potentials and did not show any correlation with the estimated $V_{1/2}$. Indeed, the relationship between $V_{1/2}$ and the R_s presents a slope not statistically different from 0 [slope = 0.05 ± 0.72 (95% CI), $R^2 = 6 \times 10^{-4}$, $n = 34$], indicating that the uncompensated R_s did not introduced any significant bias in the determination of this parameter. When recordings were obtained from electrically coupled neurons, identical voltage-clamp protocols were applied simultaneously to both cells to improve space clamp. The membrane capacitance of MesV neurons was obtained from the readout provided by the Multiclamp 700B amplifier during the procedure of cell capacitance compensation.

Activation time constants were determined by fitting the current traces evoked during voltage steps to single or double exponential functions using SciPy library from Python (https://www.scipy.org/). The uncompensated capacitive transients and activation delays occurring at the beginning of voltage commands were excluded from the fitting windows. In three representative cells, we compared the results of single versus double exponential fits. Simultaneous fitting with two exponential components yielded a fast and a slow component that presented activation time constants that averaged 0.56 ± 0.05 and 2.64 ± 0.14 s (SE), respectively, at −88.9 mV (close to the population $V_{1/2}$ of −88.5 mV, see RESULTS). However, the amplitude of the slow exponential component at this voltage step represented only 7.4% of the fast component. Accordingly, the inclusion of the second exponential term resulted in a negligible improvement of fitting in comparison to single exponential fitting as indicated by the reduction of R^2. In fact, R^2 from double exponential fittings was reduced on average by only 0.24% in comparison to R^2 from single exponential fittings at −88.9 mV and at −118 mV this reduction averaged 1.5%. On the other hand, fast time constants obtained from double exponential fits to current traces obtained in response to voltage steps ranging from −70 to −120 mV were almost indistinguishable from time constants from single exponential fits. For instance, at −88.9 mV the activation time constant averaged 0.56 ± 0.05 and 0.61 ± 0.05 s (SE), respectively ($P = 0.48$; paired, two-tailed t-test). Therefore, based on these observations and for the sake of simplicity of both fitting procedures and computational modeling, the activation time constant of the I_H was determined from single exponential fits.

Because recordings were obtained at room temperature (20–25°C) and activation kinetics is a highly temperature-dependent process (Sterratt 2014), time constants were normalized to 20°C assuming a Q_{10} of 4 (Robinson and Siegelbaum 2003).

Statistical analysis. Results were expressed as average value ± SD or means ± SE. Significance of quantitative data was determined by using χ^2-test and Student's t-test (GraphPad Software). Correlation between data sets was assessed by linear regression analysis using Igor 7 (WaveMetrics). Slope values of best-fit lines were reported as value ± 95% CIs. Two data sets were considered to be correlated if zero is not included in this confidence interval (Canavos 1988). P values for linear regression analysis was obtained using the P Value from Pearson (R) Calculator retrieved from https://www.socscistatistics.com/pvalues/pearsondistribution.aspx (Social Science Statistics, March 3, 2019).

MesV cells model and computational simulations. A reduced computational model of MesV neurons was implemented in NEURON + Python (Hines et al. 2009). This model consisted in two compartments, one representing the soma and the other the axon. The geometry of each compartment was initially set based on previous work using intracellular injections of neurobiotin (Curti et al. 2012), and final values were tuned following standard procedures by fitting exponential functions to the decay of passive voltage membrane responses to long current steps. According to that, the soma of these cells was modeled as a compartment of 25 μm in diameter and 25 μm in length connected to a cylindrical axon compartment of 3 μm in diameter and 450 μm in length [axon length was obtained after further optimization through evolutionary multiobjective optimization algorithm (EMOO; see below) due to uncertainty of axonal length after the slicing procedure].

The following six Hodgkin-Huxley type active conductances were inserted into the soma compartment: persistent sodium current (I_{NaP}) (Enomoto et al. 2007), transient sodium current (I_{NaT}) (Enomoto et al. 2007), delayed rectifier (I_{DRK}) (Del Negro and Chandler 1997), A-type potassium current [I_A (this conductance presents low activation threshold, sensitivity to 4-aminopyridine in the μM range, almost no inactivation, and most probably is mediated by Kv1.1 and Kv1.6 channels)] (Saito et al. 2006; Yang et al. 2009), high-threshold fast potassium current (I_{HT}) slightly modified from a previous report (Wang et al. 1998) and most probably mediated by Kv3.1 channels, and hyperpolarization-activated current (I_H). All these active conductances were previously described in MesV neurons except for the I_{HT}, which was included instead of the fast transient outward current ($I_{TOC\text{-}F}$) (Del Negro and Chandler 1997) to obtain spikes whose durations are consistent with experimental observations. In fact, including $I_{TOC\text{-}F}$ as the only spike repolarizing mechanism yielded action potentials with durations of ~3–4 ms at its base, which is significantly longer than the recorded spikes (~1 ms at the base and half-widths of ~450 μs; see Fig. 9*A*, *bottom*). In contrast, currents mediated by Kv3.1 channels, analog to our I_{HT} current, present rapid kinetics and a high threshold of activation consistent with the brief duration of MesV neuron's spikes, similar to neurons of the MNTB (Johnston et al. 2010; Wang et al. 1998). In addition, Kv3 subunits have been detected in MesV neurons (Saito et al. 2006). For the sake of modeling spike-based electrical transmission (essential for the study of synchronization and coincidence detection), spike duration is a critical parameter as longer than real spikes will correspond to an overrepresentation of low-frequency components of the spike power spectrum. Thus long-lasting spikes in combination with the filter frequency characteristics of electrical transmission between MesV neurons (Curti et al. 2012) would result in coupling potentials larger than normal for a given gap junction conductance.

On the other hand, the axon compartment contained the same active mechanisms as the soma except for the I_A that was not included because Kv1.1 and Kv1.6 were localized only in the somata and not in axons of MesV neurons (Saito et al. 2006).

To generate a biophysically realistic model of MesV neurons, it is necessary to know what kind of active conductances are present in each cellular compartment as well as the relative densities of these mechanisms. Despite the fact that the presence of several voltage-dependent conductances in the soma is well documented by the work of several groups, the densities of these conductances might vary according to age, sex, modulatory state, recording conditions and species among other factors. Moreover, the presence of voltage-dependent conductances in the axon is inferred mainly from morphological studies and most of them have not been directly measured experimentally. Therefore, these model parameters have been tuned to match the experimentally observed electrophysiological properties and input-output relation of MesV neurons using an EMOO) (Bahl et al. 2012) (Python library available in https://projects.g-node.org/emoo). This algorithm was applied in a step-wise manner: first, its passive properties (axon length, membrane and axial resistances), then the maximum values of subthreshold active conductances (I_{NaP}, I_A, and I_H), and finally those that operate mainly in the suprathreshold range of membrane potentials (I_{NaT}, I_{HT}, and I_{DRK}). This procedure defines a set of objective parameters [resting membrane potential, input resistance, spike characteristics (height and duration), and time constant and firing characteristics (frequency and number of spikes)], which describe the basic properties and input-output relation of neurons. On the other hand, a set of variable or free parameters like the membrane and axial resistances, axon length, time constant of I_{HT}, and maximum densities of leak- and voltage-dependent conductances are allowed to fluctuate within predetermined lower and upper search bounds during the fitting procedure to minimize the least square

difference between the real parameters obtained from recordings and the model's objective parameters (Bahl et al. 2012).

After optimization of the objective parameters, a family of 35 reduced models of MesV neurons was obtained. Electrophysiological properties of these models reasonably matched those of a sample ($n = 15$) of experimentally recorded neurons in terms of resting membrane potential [-54.7 ± 0.5 mV (SE) experimental vs. -55.2 ± 0.2 mV (SE) model, $P = 0.38$), input resistance [118.3 ± 8.1 MΩ (SE) experimental vs. 114.9 ± 1.1 MΩ (SE) model, $P = 0.54$], spike amplitude [93.3 ± 2.0 mV (SE) experimental vs. 98.6 ± 1.9 mV (SE) model, $P = 0.13$], spike duration at -20 mV [0.7 ± 0.1 ms (SE) experimental vs. 0.7 ± 0.0 ms (SE) model, $P = 0.77$], spike afterhyperpolarization level [-62.01 ± 0.7 mV (SE) experimental vs. -64.2 ± 1.1 mV (SE) model, $P = 0.23$], and frequency of the first interspike interval in response to a current step of +400 pA [119.0 ± 7.9 Hz (SE) experimental vs. 111.4 ± 3.3 Hz (SE) model, $P = 0.32$) (unpaired, two-tailed *t*-test]. Fitting parameters obtained from these simulations were averaged and fine-tuned to obtain a representative model of the MesV cells population that mimics the main characteristics of repetitive discharges in control conditions (see Fig. 9, *A–D*). The equations describing the model's membrane conductances are the following:

Leak current: $I_L = \bar{g}_L(V - E_L)$, where $\bar{g}_L = 3 \times 10^{-5}$ S/cm^2 in the soma and $\bar{g}_L = 15 \times 10^{-5}$ S/cm^2 in the axon.

Hyperpolarization-activated current: $I_h = \bar{g}_h n_h(V - E_h)$, where $n_{h\infty}(V) = \left(1 + e^{\frac{V+89}{8}}\right)^{-1}$ and $\tau_h(V) = 417\left(1 + \left(\frac{V+70}{4}\right)^2\right)^{-1} +$ 366 ms, $\bar{g}_L = 6 \times 10^{-4}$ S/cm^2

A-type potassium current: $I_A = \bar{g}_A n_A(V - E_K)$, where $n_{A\infty}(V) = \left(1 + e^{-\frac{V+48}{4}}\right)^{-1}$, $\tau_A = 3.4$ ms, $\bar{g}_L = 1 \times 10^{-3}$ S/cm^2

Delayed rectifier potassium current: $I_{DRK} = \bar{g}_{DRK} n_{DRK}(V - E_K)$, where $n_{DRK}(V) = \left(1 + e^{-\frac{V+4.2}{12.9}}\right)^{-1}$, $\tau_{DRK}(V) = 25\left[(1 + e^{-\frac{V+40}{15}}\right)^{-1} + \left(1 + e^{\frac{V-25}{2}}\right)^{-1}\Big] - 23$ ms, $\bar{g}_{DRK} = 1.3 \times 10^{-4}$ S/cm^2

High-threshold fast potassium current: $I_{HT} = \bar{g}_{HT} m_{HT}^3(V - E_K)$, where $m_{HT\infty}(V) = \left(1 + e^{-\frac{V-5}{15}}\right)^{-1}$, $\tau_{HT}(V) = 0.5 + 0.6\left(1 + e^{-\frac{V+57}{31}}\right)^{-1}$ ms, $\bar{g}_{HT} = 1.2 \times 10^{-1}$ S/cm^2

Persistent sodium current: $I_{NaP} = \bar{g}_{NaP} n_{NaP\infty}(V - E_{Na})$, where $n_{Nap\infty}(V) = \left(1 + e^{-\frac{V+50}{5.3}}\right)^{-1}$, $\bar{g}_{NaP} = 1.8 \times 10^{-5}$ S/cm^2

Transient sodium current: $I_{NaT} = \bar{g}_{NaT} m_{NaT}^3 h_{NaT}(V - E_{Na})$, where $m_{NaT\infty}(V) = \left(1 + e^{-\frac{V+24}{5.5}}\right)^{-1}$, $\tau_{mNaT}(V) = 0.2$ ms, $h_{NaT\infty}(V) = \left(1 + e^{\frac{V+77}{8.6}}\right)^{-1}$, $\tau_{hNaT}(V) = 0.3 + 5e^{-\frac{V+50}{10}}$ ms, $\bar{g}_{NaT} = 8 \times 10^{-2}$ S/cm^2

The corresponding reversal potentials are $E_h = -28.7$ mV, $E_K = -93.0$ mV, $E_{Na} = 78.0$ mV, and $E_L = -58$ mV.

The effects of cGMP on I_H current were simulated by modifying the parameters describing the activation at steady state ($V_{1/2}$, K, and $\bar{g}_h$), as well as its kinetics consistently with experimental results. Accordingly, the equation describing the modulated I_H current is the following:

$I_h = \alpha \bar{g}_h n_h(V - E_h)$, where $n_{h\infty}(V) = \left(1 + e^{\frac{V+83.1}{9.7}}\right)^{-1}$, $\tau_h(V) = 296e^{-\left(\frac{V+75.4}{17.4}\right)^2} + 42$ ms and $\alpha = 1.26$.

Small networks consisting of pairs of coupled MesV neurons were simulated as two identical representative model neurons connected by a voltage independent conductance in agreement with previous results obtained in this neuronal population (Curti et al. 2012). The value of this conductance representing gap junctions was 4 nS also in agreement with our previous work and the equation describing these electrical contacts is the following:

$$I_{jpre \to post} = g_j(V_{post} - V_{pre})$$

where g_j is the gap junction conductance and V_{post} and V_{pre} are the membrane potentials of the post- and presynaptic cells, respectively.

RESULTS

Coincidence detection between pairs of electrically coupled MesV neurons is heterogeneous. We previously reported that pairs of electrically coupled MesV neurons may be highly susceptible to synchronic or coincident depolarizing inputs. In fact, simultaneous depolarizations tend to be much more efficient in evoking repetitive discharges in comparison to temporally distributed inputs (Curti et al. 2012). This phenomenon, herein referred to as coincidence detection, is illustrated in Fig. 1 for a pair of electrically coupled neurons (Fig. 1*A*), where depolarizing current pulses evoked only one or two spikes when applied alternatively to each cell (Fig. 1*B*, *left* and *middle*), whereas simultaneously applied current pulses of the same intensity evoke repetitive discharges in both cells (Fig. 1*B*, *right*). The number of spikes when cells were coactivated is significantly higher than when cells were activated in isolation averaging 5.56 ± 0.78 and 1.51 ± 0.13 (SE), respectively ($P = 1 \times 10^{-4}$; $n = 76$ from 38 pairs, paired, two-tailed *t*-test; Fig. 1*C*, black circles), confirming that pairs of coupled MesV neurons behave as coincidence detectors. To quantify this property, a coincidence detection index (coincidence detection index) was calculated (see MATERIALS AND METHODS). This index, calculated as the difference in spike number when stimuli were delivered simultaneously to both cells or individually to each one, represents the gain of coincidence detection or susceptibility to coincident inputs and has units of spikes. The coincidence detection index for the population of coupled neurons ($n = 76$ from 38 pairs) averaged 4.05 ± 0.74 spikes (SE) (Fig. 1*D*). In contrast, when the same stimulation protocol was applied to pairs of MesV neurons whose cell bodies were juxtaposed but electrically uncoupled (Fig. 1*E*), neuronal firing evoked by individual and coincident stimulation showed no differences, averaging 1.70 ± 0.37 and 1.85 ± 0.49 (SE), respectively ($P = 0.76$; $n = 20$ from 10 pairs, paired, two-tailed *t*-test; Fig. 1, *F* and *G*). Consistently, the coincidence detection index of uncoupled cells averaged 0.15 ± 0.48 spikes (SE). These results support the idea that electrical coupling is indispensable for coincidence detection between MesV neurons.

Electrical coupling represents an attribute that divides the population of MesV neurons in seemingly homogeneous categories in terms of their computational capabilities; that is, those that are able to detect coincident inputs from those that are not. However, coincidence detection among coupled neurons is diverse. Indeed, the plots of the number of spikes according to the stimulation protocol, independent versus simultaneous depolarizations, display a great diversity of slopes (Fig. 1*C*, gray circles). The slope of these plots is indicative of how cells perform as coincidence detectors, being directly proportional to the coincidence detection index. Consistently, the coincidence detection index in control conditions ranges between ~0 and 31 spikes confirming that coincidence detection in terms of its gain is highly heterogeneous across the population of MesV neurons (Fig. 1*D*).

Coincidence detection gain critically depends on the intrinsic excitability of coupled neurons. As shown, coincidence detection between MesV neurons depends on electrical cou-

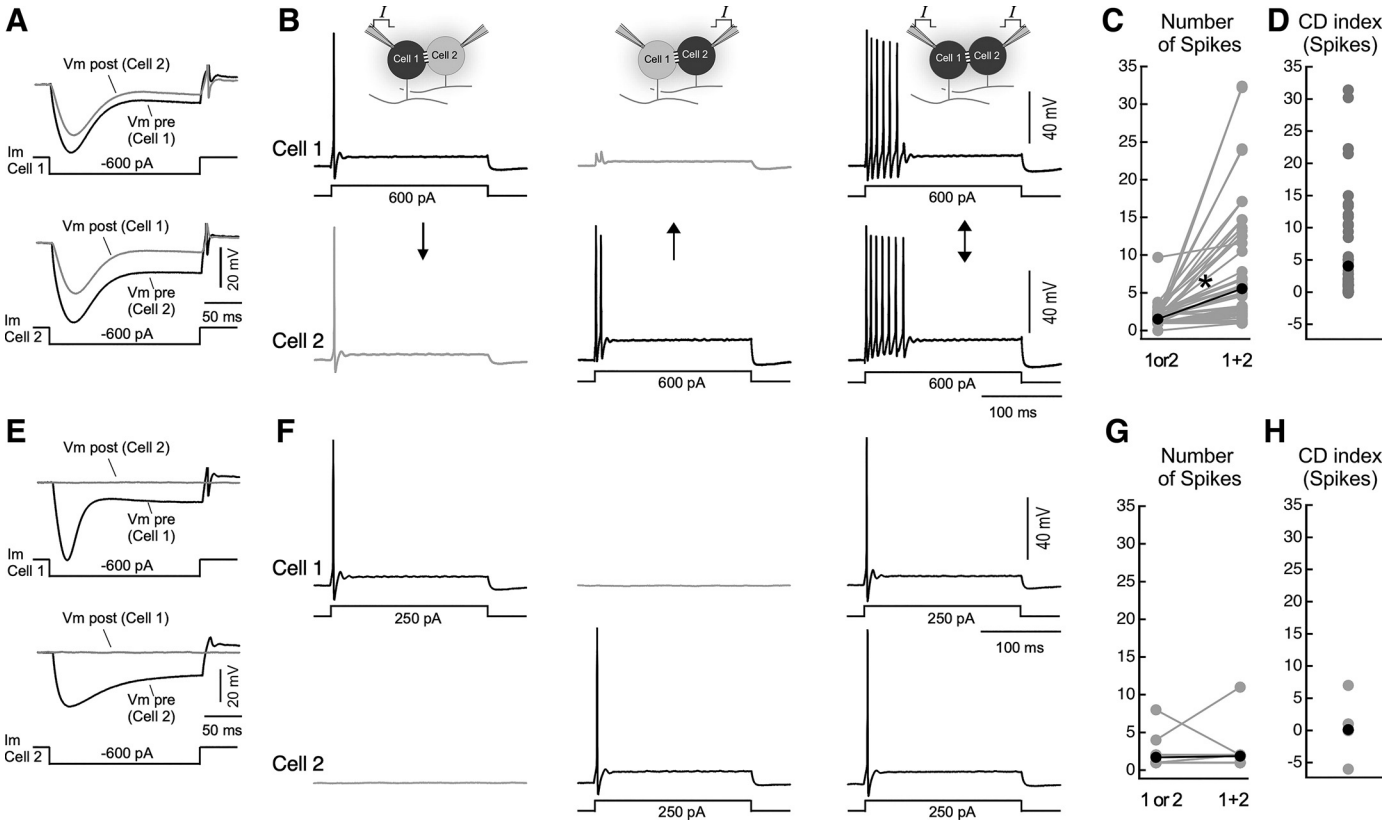

Fig. 1. Electrical coupling between mesencephalic trigeminal (MesV) neurons supports coincidence detection. *A*: simultaneous membrane voltage (V_m) responses to hyperpolarizing current (I_m) pulses injected either in *cell 1* (*top*) or in *cell 2* (*bottom*) of a pair of adjacent coupled neurons. *B*: in the same pair of neurons, injection of a depolarizing current pulse in *cell 1* (*left*) or *cell 2* (*middle*) induced a brief response consisting of 1 or 2 spikes at the beginning of the current step, with their corresponding coupling potentials (spikelet) in the coupled cell. Simultaneous activation of these 2 neurons with the current pulses of the same magnitude (*right*) evoked instead a repetitive discharge at each cell, consisting of 6–7 spikes. Schemes above each set of traces indicate the stimulation protocol. *C*: plot of the number of spikes when cells were independently activated (*1* or *2*) and when simultaneously activated (*1 + 2*) for the sample of recorded coupled neurons. Values represented by gray circles correspond to the average number of spikes evoked by 20 consecutive identical current pulses to each recorded cell belonging to a coupled pair. Superimposed are illustrated the average values (black circles) for the population of recorded neurons ($P = 1 \times 10^{-4}$; $n = 76$ from 38 pairs recorded in 32 animals, paired, two-tailed *t*-test). *Significant difference, $P < 0.05$. *D*: plot of the coincidence detection (CD) index calculated as the mean difference of the number of spikes when cells are simultaneously activated (*1 + 2*) minus when independently activated (*1* or *2*) for the same sample illustrated in *C*. Individual values (gray circles) and the average value for the whole sample (black circle) are superimposed. *E*: simultaneous membrane voltage responses to hyperpolarizing current pulses injected either in *cell 1* (*top*) or in *cell 2* (*bottom*) of a pair of adjacent uncoupled neurons. *F*: in the pair of neurons depicted in *E*, membrane voltage responses of both cells when depolarizing current pulses were injected in *cell 1* or in *cell 2* (*left* and *middle*, respectively) and when current pulses were simultaneously injected to both cells (*right*). *G*: plot of the number of spikes when cells were independently activated (*1* or *2*) and when simultaneously activated (*1 + 2*) for the sample of recorded uncoupled neurons. Values from individual cells (gray circles) and average values (black circles) for the population of recorded neurons ($P = 0.76$; $n = 20$, from 10 pairs, 8 animals, paired, two-tailed *t*-test) are illustrated superimposed. *H*: plot of the CD index for the same sample illustrated in *G*.

pling, raising the possibility that the heterogeneity of this network operation results from the diversity of coupling strengths in our sample of recorded pairs. However, surprisingly, the coincidence detection index and the CC in the forward direction (from the cell under consideration to its coupled partner) did not show any correlation as indicated by linear regression analysis [slope = 6.50 ± 8.13 (95% CI), $R^2 = 0.033$, $P = 0.12$; Fig. 2*A*]. This analysis using CC in the opposite direction would yield similar results as electrical transmission between MesV neurons is highly bidirectional (Curti et al. 2012). To gain direct insights into the determinants of such heterogeneity, we focused on the study of the loading effect. In fact, the contrast in firing between individual and simultaneous depolarizations, corresponding to the gain of coincidence detection, is caused by larger depolarizations of the membrane potential, due to the cancelation of the loading effect during simultaneous inputs in comparison to when inputs arrive independently (Fig. 2*B*). We estimated the loading effect (the impact on input resistance due to coupled cells) in a subset of neurons as we did previously (Curti et al. 2012). The input resistance (*Rin*) of cells belonging to coupled pairs was measured by applying hyperpolarizing current pulses, either individually to each cell or simultaneously to both cells (Fig. 2*C*, *left*). Form these recordings, current-voltage curves were constructed and *Rin* values were estimated from the slope of linear regressions (Fig. 2*C*, *right*). Simultaneous pulse protocols yielded significantly higher *Rin* values than those obtained with individual stimulation, averaging 118.3 ± 6.84 and 86.6 ± 5.88 MΩ (SE), respectively ($P = 9 \times 10^{-5}$; $n = 26$, paired, two-tailed *t*-test). From these values, the loading effect in each cell was quantified as the difference of *Rin* obtained with these two protocols, expressed as percentage of the *Rin* obtained with individual pulses (loaded condition). This value averaged 39.6 ± 3.06% (SE) for the population of studied neurons ($n = 26$ from 13 pairs; Fig. 2*D*), and individual values present a positive correlation with the

CC in the forward direction [slope of linear regression = 69.3 ± 24.2 (95% CI), $R^2 = 0.59$, $P < 1 \times 10^{-5}$; Fig. 2*E*] consistent with our previous work (Curti et al. 2012). We reasoned that if the loading effect would be the only or main mechanism involved in coincidence detection, the susceptibility of coupled neurons to simultaneous inputs (measured as the coincidence detection index) should be proportional to the magnitude of the loading effect. Surprisingly, these two data sets did not show any correlation [slope of linear regression = 0.12 ± 0.14 (95% CI), $R^2 = 0.1$, $P = 0.107$; Fig. 2*F*]. In fact, neurons with comparable loading effect magnitude can perform quite different as coincidence detectors (Fig. 2*F*, purple circles) and conversely, neurons with dissimilar loading effect can perform similar in terms of coincidence detection gain (Fig. 2*F*, green circles). These results indicate that the gain of coincidence detection cannot be explained solely in

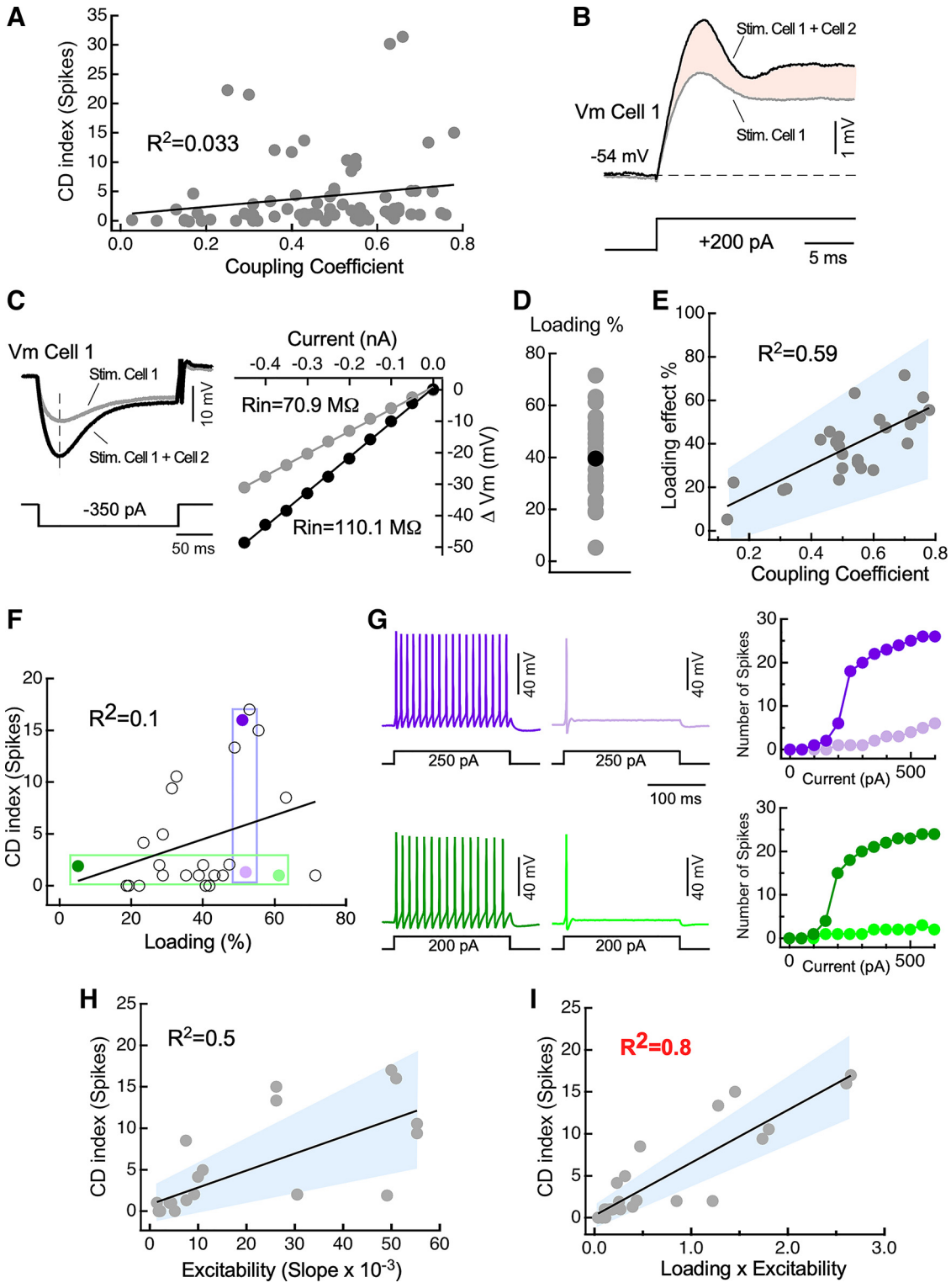

terms of the magnitude of the loading effect and suggest the involvement of other mechanisms. On the other hand, the loading effect not only depends on the coupling strength but also on the number of cells each neuron is connected to (Getting 1974). However, the MesV nucleus is organized almost exclusively in pairs of cells (pairs ~90%, triplets ~10%) (Curti et al. 2012), ruling out the possibility that the heterogeneity in coincidence detection resulted from differences in the size of networks of coupled neurons.

Because neuronal spiking represents the functional expression of coincidence detection, the intrinsic excitability of neurons may also play, along with the loading effect, a relevant role in determining the susceptibility of coupled neurons to coincident inputs. Coincidently, MesV neuron excitability displays great variety even at comparable ages. Indeed, neuronal responses range from single spikes at the beginning of current pulses, regardless of the stimulation intensity, to strong repetitive discharges (see below), possibly contributing to the heterogeneity of coincidence detection gain. In fact, comparison of the cells indicated by purple circles in Fig. 2*F* (loading effect of similar magnitude, ~50%) reveals that the one presenting higher susceptibility to coincident inputs (coincidence detection index = 16 spikes, dark purple circle) is also the more excitable one as indicated by its firing properties (Fig. 2*G*, compare dark and light purple traces and curves in the *top*). On the other hand, the cells, indicated by green circles in Fig. 2*F*, are comparable in terms of their susceptibility to coincident inputs (coincidence detection index between 1 and 2 spikes), in spite of presenting quite dissimilar loading effect (5 vs. 61%). Strikingly, the neuron with the lower loading effect magnitude presents stronger spiking in comparison to the neuron with the higher loading (Fig. 2*G*, compare dark and light green traces and curves in the *bottom*). In this case, neuronal excitability seems able to compensate for differences in loading effect, suggesting a relevant role of firing properties. Consistently, neuronal excitability, quantified as the slope of curves of the number of spikes versus current (see MATERIALS AND METHODS), is positively correlated with the coincidence detection index [slope of linear regression = 204.9 ± 85.8 (95% CI), R^2 = 0.5, $P = 5 \times 10^{-5}$; Fig. 2*H*]. Moreover, when the excitability is weighted by the loading effect (calculated as the product of these 2 variables), the fit to a straight line improves considerably [slope of linear regression = 6.29 ± 1.34 (95% CI), $R^2 = 0.8$, $P < 1 \times 10^{-5}$; Fig. 2*I*]. These results indicate that while electrical coupling is absolutely necessary for coincidence detection to occur, the intrinsic excitability of neurons critically contributes to set the gain of this relevant functional operation in networks of coupled neurons. Therefore, the heterogeneity of coincidence detection gain does not result solely from differences in coupling strengths but also from the diversity of the intrinsic excitability of coupled neurons.

Regulation of the I_H as a way to modulate MesV neuron excitability. Our results suggest that the firing properties of coupled neurons play a critical role in determining the gain of coincidence detection, raising the possibility that its heterogeneity resulted in part from the diverse regulatory states of intrinsic electrophysiological properties across the population of MesV neurons. Hence, modulations of firing properties are good candidates to mediate forms of plasticity that alter the way coupled neurons respond to coincident inputs. To test this, we sought to modulate the excitability of MesV neurons by way of upregulating the I_H through applications of cyclic nucleotides (Biel et al. 2009). The I_H is a widespread current in the mammalian brain, which operates in the subthreshold range of membrane potential and has been shown to be critically involved in repetitive discharges, rhythmic oscillatory activity, and integration of synaptic inputs (Pape 1996). On the other hand, the I_H is a common feature of many populations of electrically coupled neurons, like inferior olive neurons (Devor and Yarom 2002; Schweighofer et al. 1999), GABAergic neurons of thalamic reticular nucleus (Landisman et al. 2002; Rateau and Ropert 2006), pyramidal neurons from the hippocampus (Maccaferri et al. 1993; Mercer et al. 2006) and neocortex (Trenholm et al. 2013; Wang et al. 2010), Golgi cells of the cerebellar cortex (Dugué et al. 2009; Forti et al. 2006), bipolar cells of the retina (Müller et al. 2003; Veruki and Hartveit 2002b), and mitral cells of the olfactory bulb (Angelo and Margrie 2011; Schoppa and Westbrook 2002) among others. The coexistence of this conductance and electrical synapses raises the possibility of functional interaction between them as suggested by a theoretical study (Publio et al. 2009).

Fig. 2. Coincidence detection (CD) between pairs of electrically coupled mesencephalic trigeminal (MesV) neurons is heterogeneous. *A*: plot of CD index against the coupling coefficient for the whole sample of recorded coupled MesV neurons (n = 76 from 38 pairs recorded in 32 animals). Slope of linear regression = 6.5 ± 8.13 [95% confidence interval (CI)] represented by the continuous line; $R^2 = 0.033$, $P = 0.12$. *B*: superimposed are representative traces showing membrane voltage (V_m) responses when subthreshold current pulses were injected only into the recorded neuron (*stim. cell 1*, gray trace) or simultaneously to both coupled neurons (*stim. cells 1 + 2*, black trace). Solid pink area represents the difference between these 2 stimulation protocols, corresponding to the increase in membrane responses due to the cancelation of the loading effect during coincident depolarizations. *C*, *left*: estimation of the loading effect in coupled cells by injecting hyperpolarizing current pulses, either individually to each cell (*stim. cell 1*, gray trace) or simultaneously to both cells (*stim. cell 1 + cell 2*, black trace). *C*, *right*, from these recordings, change in membrane voltage versus current relationships were constructed for both individual (gray circles) and simultaneous (black circles) stimulation protocols. Membrane voltage changes were measured at the time indicated by the vertical dashed line at *left*. Continuous lines represent best fit to straight-line functions and slopes, corresponding to input resistance (*Rin*) values, are indicated. *D*: plot of the loading effect values (see text) measured in 26 coupled neurons. Superimposed to values from individual cells (gray circles) is the average value (black circle). *E*: plot of the loading effect against the coupling coefficient in the same neuronal population depicted in *D*. Slope of linear regression = 69.3 ± 24.2 (95% CI), represented by the continuous line; $R^2 = 0.59$, $P < 1 \times 10^{-5}$, n = 26. *F*: plot of the CD index as a function of the loading effect. Slope of linear regression = 0.12 ± 0.14 (95% CI), represented by the continuous line; $R^2 = 0.1$, $P = 0.107$, n = 26. Representative cells displaying nearly the same loading effect magnitude (purple tones) and coincidence detection index (green tones) are boxed. *G*, *left*: traces of voltage membrane responses to depolarizing current pulses (250 pA) of the neurons indicated in *F* with purple tones (similar loading effect, above) and with green tones (similar CD index, below). *G*, *right*: plots of the number of spikes evoked by current pulses of 200 ms in duration as a function of the current intensity for the cells shown at *left*. The same color code (purple/green, dark/light) applies in *F* and *G* for the identification of corresponding neurons. *H*: plot of the CD index against neuronal excitability (quantified as the slope of spikes vs. current curves). Slope of linear regression = 204.93 ± 85.8 (95% CI), represented by the continuous line; $R^2 = 0.5$, $P = 5 \times 10^{-5}$, n = 26. *I*: plot of the CD index (ordinates) against the product of the loading effect magnitude times the slope of spikes versus current curves (loading × excitability, abscissa). Slope of linear regression = 6.2863 ± 1.34 (95% CI), represented by the continuous line; $R^2 = 0.8$, $P < 1 \times 10^{-5}$, n = 26. In *E*, *H*, and *I*, the solid blue area represents the 95% confidence interval. Plots in *D*, *E*, *F*, *H*, and *I* show results obtained in the same neuronal population (n = 26, from 13 pairs recorded in 10 animals).

MesV neurons also express a prominent I_H (Khakh and Henderson 1998) that contributes to stabilize the resting membrane potential and control cell excitability (Tanaka et al. 2003). Moreover, the channel-forming subunits HCN1 and HCN2 have been detected and present a somatic distribution in this neuronal population (Kang et al. 2004; Notomi and Shigemoto 2004). Consistent with that, voltage responses more negative than −70 mV are dominated by a prominent sag (Fig. 3*A*), which are almost completely abolished after the addition of CsCl (2 mM) to the extracellular solution (Fig. 3*B*). On the other hand, an important characteristic of I_H is its ability to be regulated by cyclic nucleotides like cAMP and cGMP with relevant consequences on the electrophysiological properties of neurons (Biel et al. 2009; Lüthi and McCormick 1998; Pape 1996), thus representing a potentially valuable tool to manipulate the intrinsic excitability of MesV neurons.

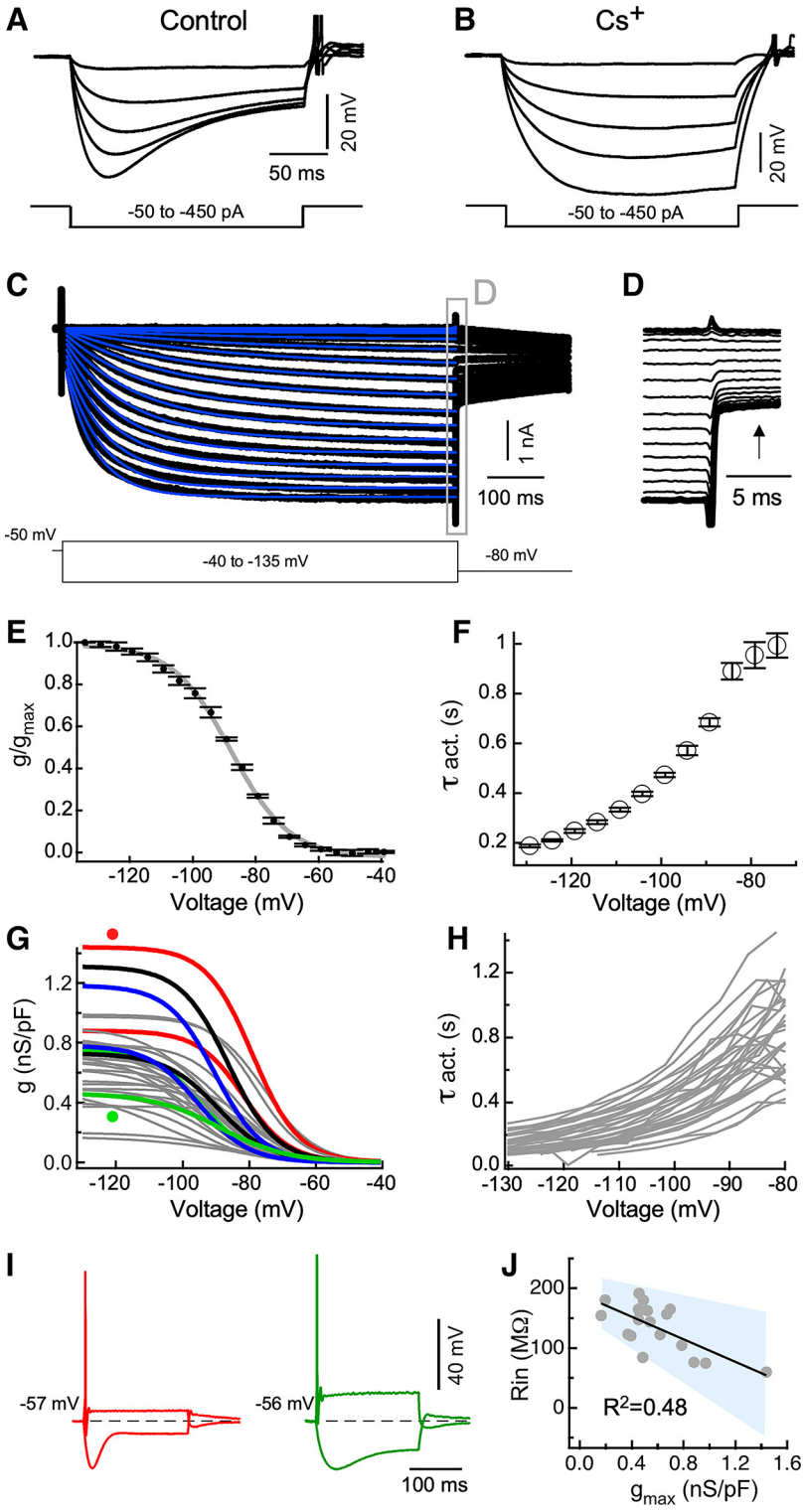

Fig. 3. Characterization of hyperpolarization-activated cationic current (I_H) of mesencephalic trigeminal (MesV) neurons. *A*: representative traces of membrane voltage responses of a MesV neuron in control conditions to a series of hyperpolarizing current pulses of different intensities from −50 to −450 pA in steps of 100 pA: *B*: same cell and current injecting protocol as in *A* after the addition of 2 mM CsCl to the bath. *C*: sample traces of the I_H evoked with a series of voltage steps from −135 to −40 mV, in 5-mV increments, from a holding potential of −50 mV, and followed by a test pulse to −80 mV. Each trace represents the subtraction of total membrane currents obtained in the presence of Cs^+ from those obtained in control conditions. A scheme of the voltage-clamp protocol is at *bottom*. *D*: the boxed area in *C* is illustrated at an expanded temporal scale. *E*: I_H steady-state activation curve of the cell depicted in *C* and *D*, obtained by plotting the normalized conductance against the voltage pulse commands. Conductance values (g) were determined from tail currents measured at the time indicated by the upward arrow in *D*. Each value represents the average of 4 single values obtained in the same cell and error bars represent SD. Experimental data were fit to a Boltzmann function (gray trace). *F*: plot of the I_H activation time constant (τ act.) of the cell shown in *C* against the voltage pulse commands. The activation kinetics was determined by fitting exponential functions to the activation phase of current traces evoked by different voltage commands (superimposed blue traces in *C*). Each value represents the average of 4 single values obtained in the same cell, and error bars represent SD. *G*: plot of Boltzmann function fits to I_H steady-state activation curves of the whole sample of recorded neurons (n = 33 recorded in 17 animals). Note that conductance values were normalized to the cell's capacitance for comparing neurons of different sizes. Curves from 4 animals are colored (red, green, blue, and black) to illustrate that variety of I_H expression results from both inter- and intraindividual diversity. *H*: plot of activation time constant against voltage pulse commands of the same neurons depicted in *G*. *I*: membrane voltage responses to depolarizing and hyperpolarizing current pulses of cells identified by filled circles of the same color in *G*. *J*: plot of the input resistance (*Rin*) against the I_H maximum density in a sample of 19 uncoupled MesV neurons recorded in 10 animals. Slope of linear regression = −94.5 ± 50.4 (95% CI), represented by the continuous line; R^2 = 0.48, P = 0.001. The solid blue area represents the 95% confidence interval.

We started by characterizing the I_H of MesV neurons in control conditions by applying standard protocols in voltage clamp (see MATERIALS AND METHODS). Figure 3*C* shows representative results from one neuron, in which I_H was recorded in voltage clamp, during protocols consisting in a series of voltage steps from −40 to −135 mV starting from a holding potential of −50 mV and returning to a potential of −80 mV. Stepping negative to −70 mV elicited an inward current with slow activation kinetics and no signs of inactivation within this time window that also deactivates with a slow time course. Figure 3*E* depicts the activation curve obtained from these recordings. This curve was constructed by measuring tail currents at the time indicated by the upward arrow in Fig. 3*D* at a constant membrane voltage of −80 mV. Superimposed are the conductance values normalized to its maximum (black circles) and the fit to a Boltzmann function (gray trace) (Fig. 3*E*). For the whole population of recorded neurons ($n = 34$), fits of the Boltzmann relation to activation curves showed that the $V_{1/2}$ averaged −88.5 ± 1.17 mV (SE), with a slope factor of 8.4 ± 0.29 mV (SE). Maximal conductance averaged 30.9 ± 2.8 nS (SE) and when normalized to the cell's capacitance averaged 0.68 ± 0.05 nS/pF (SE). Activation kinetics of the I_H was determined from the fits of single exponential functions to current traces (superimposed blue traces on Fig. 3*C*). Plots of the activation time constant as a function of the voltage step showed the typical behavior characterized by a progressive lowering of the time constant (faster activation) with increasing hyperpolarized voltage steps (Fig. 3*F*). Maximal time constant averaged 938.7 ± 52.8 ms (SE) and occurred at voltage steps ranging from −68 to −88.4 mV (average −78.8 mV). Interestingly, steady-state activation characteristics and activation kinetics showed considerable variety across the population of recorded neurons. Figure 3*G* shows superimposed results of fits to activation curves for the whole sample of recorded neurons ($n = 34$), where maximal conductance ranged almost over an order of magnitude (from 0.17 to 1.44 nS/pF) whereas the $V_{1/2}$ did so over more than 30 mV (from −74.9 to −106.5 mV). Note that as conductance is normalized by the cell's capacitance, the diversity in maximal conductance values does not result from differences in the cell sizes of our sample. Interestingly, this diversity is the outcome of both interindividual and intraindividual differences, as can be appreciated in Fig. 3*G* where curves from four animals are indicated in colors (red, green, blue, and black). To support this conclusion, we computed the difference in maximal conductance between 15 pairs of cells recorded from 15 animals and compared it to the difference between pairs obtained by combining cells from different animals ($n = 210$). These values, indicative of I_H diversity, were similar and showed no statistical difference. In fact, intraindividual difference averaged 0.22 ± 0.045 nS/pF (SE) ($n = 15$), whereas interindividual difference averaged 0.31 ± 0.018 nS/pF (SE) ($n = 210$) ($P = 0.058$, unpaired, two-tailed *t*-test).

On the other hand, as expected, neurons presenting high I_H density display large amplitude sag potentials (activation curves from cells depicted in Fig. 3*I* are identified in Fig. 3*G* with circles of the same color). Also, I_H density presents a negative correlation with the *Rin* value [slope of linear regression = −94.5 ± 50.4 (95% CI, $P = 0.001$), $R^2 = 0.48$; Fig. 3*J*], suggesting the involvement of this conductance in the determination of MesV neuron passive properties.

Additionally, activation kinetics also showed considerable variety, as can be appreciated in Fig. 3*H* where curves of the time constant as a function of the voltage step for all recorded cells are shown superimposed. In fact, the maximal time constant ranged from 401 to 1,657 ms. These results indicate that I_H presents a great diversity of functional states across the population of MesV neurons, suggesting that this conductance is under regulatory control, which in turn could contribute to the diversity of intrinsic excitability displayed by this population.

We next explored if the I_H of MesV neurons is susceptible of modulation by cGMP applying its membrane permeable analogue 8-bromoguanosine cyclic 3',5'-monophosphate sodium salt (0.5–1 mM, herein referred simply as cGMP; Fig. 4). Of the two most common cyclic nucleotides, cAMP and cGMP, the latter was chosen in an attempt to selectively modulate I_H (see later), as in MesV neuron activation of the cAMP/protein kinase A signaling pathway participates in the regulation of the persistent sodium current (Tanaka and Chandler 2006). As expected, cGMP applications resulted in a shift of the $V_{1/2}$ toward positive values, as well as an increase of the I_H magnitude (Fig. 4, *A* and *B*) and acceleration of activation kinetics (Fig. 4*C*). For the sample of recorded cells ($n = 13$), the $V_{1/2}$ changed from −89.8 ± 1.4 mV (SE) in control conditions to −82.9 ± 20.8 mV (SE) after cGMP ($P = 0.0015$; paired, two-tailed *t*-test; Fig. 4*D*), whereas the slope factor increased from 8.2 ± 0.2 mV (SE) in control to 10.4 ± 0.74 mV (SE) after cGMP ($P = 0.0061$; paired, two-tailed *t*-test; Fig. 4*E*) and the maximal conductance showed an increase from 0.68 ± 0.05 nS/pF (SE) in control to 0.81 ± 0.06 nS/pF (SE) after cGMP ($P = 0.0049$; paired, two-tailed; Fig. 4*F*). Remarkably, the combined effect of cGMP on $V_{1/2}$, slope and maximal conductance resulted in an almost threefold increase in the I_H conductance at −70 mV, a membrane voltage level close to the postspike afterhyperpolarization. In fact, I_H conductance at −70 mV increased from 0.07 ± 0.017 nS/pF (SE) in control to 0.2 ± 0.043 nS/pF (SE) after cGMP ($P = 0.0066$; paired, two-tailed *t*-test). On the other hand, I_H activation kinetics becomes faster after cGMP for almost the whole range of voltage steps (Fig. 4*C*) as indicated by the significant reduction of the maximal time constant, which varied from 814.1 ± 86.6 ms (SE) in control to 623.7 ± 59.9 ms (SE) after cGMP ($P = 0.0015$; paired, two-tailed *t*-test; Fig. 4*G*). Interestingly, this change in activation kinetics favors the involvement of the I_H during the time course of the interspike interval. These results show that the I_H of MesV neurons is strongly modulated by cGMP.

Upregulation of the I_H increases MesV neuron excitability. Next, we studied the impact of I_H upregulation on MesV neuron excitability. For this, the effects of cGMP applications on the electrophysiological properties of these neurons were characterized by applying protocols of depolarizing current pulses whose intensity were adjusted to evoke one to three spikes (Fig. 5*A*, *left*). As illustrated in Fig. 5*A*, *right*, after inclusion of cGMP in the bath, there was an increase in the number of spikes evoked by current pulses in comparison to control conditions, and this effect was accompanied by a depolarizing shift of the resting membrane potential. These effects can be better appreciated in Fig. 5*B*, in which the number of spikes during current pulses repeated every 10 s and the resting membrane potential were plotted as a function of

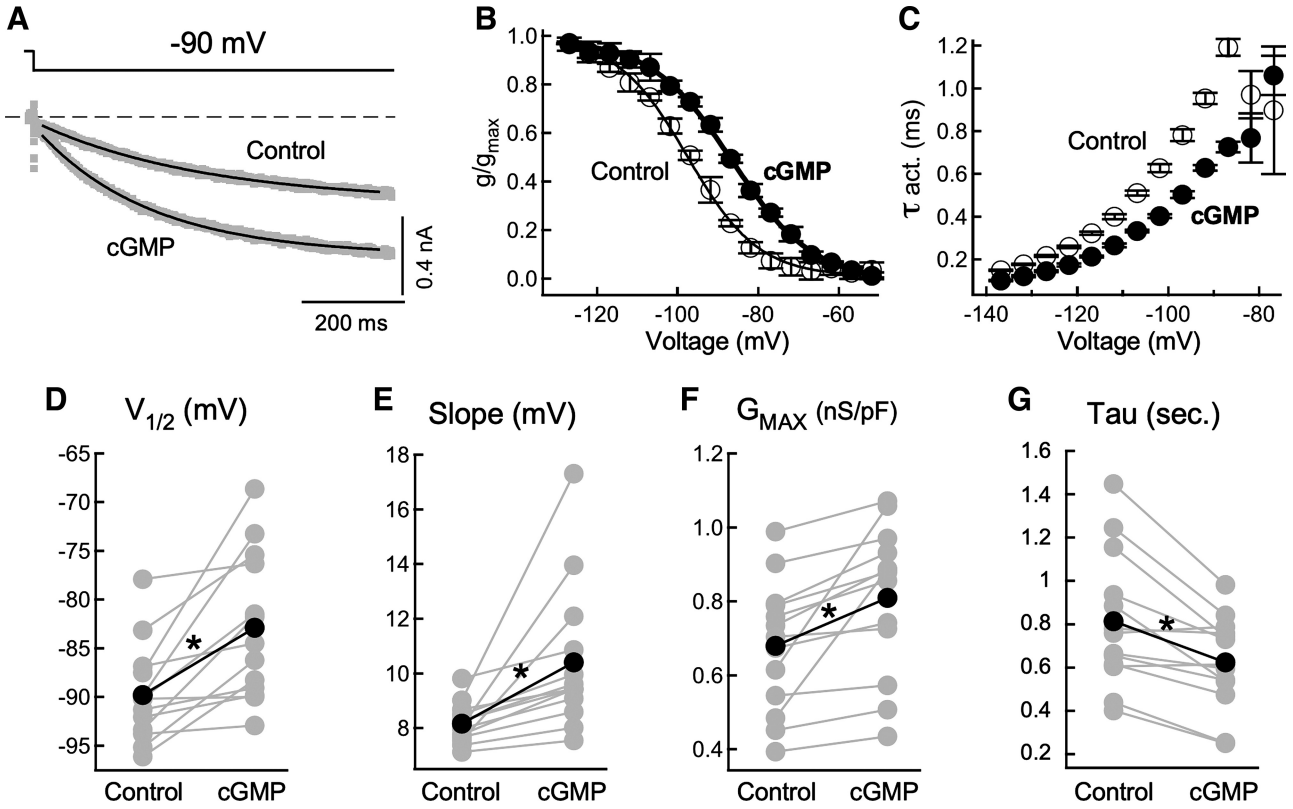

Fig. 4. Hyperpolarization-activated cationic current (I_H) of mesencephalic trigeminal (MesV) neurons is strongly modulated by cGMP. *A*: sample current traces evoked with voltage steps from −50 mV to −90 mV in control conditions (gray trace, control) and after cGMP (gray trace, cGMP). Superimposed are fits to exponential functions (black traces). *B*: I_H steady-state activation curve of the cell shown in *A* before (white circles, control) and after cGMP (black circles, cGMP). Each curve was fitted with Boltzmann functions, and results are shown superimposed (continuous traces). Each value represents the average of 4 (control) or 3 (cGMP) single values obtained in the same cell and error bars represent SD; *g*, conductance. *C*: plot of the I_H activation time constant of the cell shown in *A* against the voltage pulse commands before (white circles, control) and after cGMP (black circles, cGMP). *D*: plot of the half activation voltage ($V_{1/2}$) values of the Boltzmann function before (gray circles) and after cGMP (gray circles) for the whole population of recorded MesV neurons, ($P = 0.0015$; paired, two-tailed *t*-test, $n = 13$). *E*: plot of the slope values of the Boltzmann function at $V_{1/2}$ before (gray circles) and after cGMP (gray circles) for the whole population of recorded MesV neurons, ($P = 0.0061$; paired, two-tailed *t*-test, $n = 13$). *F*: plot of the maximal conductance values normalized to the cell's capacitance before (gray circles) and after cGMP (gray circles) for the whole population of recorded MesV neurons, ($P = 0.0049$; paired, two-tailed, $n = 13$). *G*: plot of the maximum activation time constant (determined from current traces evoked by voltage steps of −70 to −90 mV) before (gray circles) and after cGMP (gray circles) for the whole population of recorded MesV neurons, ($P = 0.0015$; paired, two-tailed *t*-test, $n = 13$). Plots in *D*, *E*, *F*, and *G* show results obtained in the same neuronal population ($n = 13$, recorded in 7 animals). Superimposed to the individual values are the corresponding average values in control (black circle) and after cGMP (black circle). *Significant difference, $P < 0.05$.

time before, during, and after bath application of cGMP (1 mM). Most typically, the maximum effects on firing and resting potential were attained between 15 and 20 min after initiation of perfusion and were long lasting as reversion was rarely observed, consistently with findings by others (Ingram and Williams 1996). A detailed characterization of cGMP effects on firing was performed by using experimental protocols consisting on a series of depolarizing current pulses of increasing intensity (50 to 600 pA; Fig. 5*C*). From these experiments, plots of the number of spikes as a function of injected current were constructed (Fig. 5*D*). These plots show a dramatic increase of firing particularly for current pulses of twice the threshold intensity and above. The average behavior of our sample can be seen in Fig. 5*E*, in which the mean number of spikes was plotted as a function of current pulse intensity before (control) and after cGMP application. This graph shows that cGMP induces a statistically significant increase ($P < 0.01$) in the number of spikes for most of the current pulses tested, indicating a dramatic increase in MesV neurons excitability and hence in the way this neuronal population encode depolarizing inputs. Consistently, the threshold current for spike activation was reduced from 171.1 ± 19.6 pA (SE) in control conditions to 147.4 ± 15.2 pA (SE) after cGMP ($P = 0.016$, $n = 19$, paired, two-tailed *t*-test).

The number of spikes per current pulses of three- to sixfold its threshold intensity (determined in control conditions) showed an increase from 2.9 ± 0.68 (SE) in control to 8.7 ± 1.55 (SE) after cGMP, and this difference was statistically significant ($P = 5.9 \times 10^{-5}$; $n = 30$, paired, two-tailed *t*-test). Additionally, the resting membrane potential varied from −59.3 ± 0.88 mV (SE) in control to −54.5 ± 0.73 mV (SE) after cGMP ($P = 2.3 \times 10^{-9}$; $n = 30$, paired, two-tailed *t*-test; Fig. 5*F*). These effects did not show any significant difference in coupled versus uncoupled cells. The average number of spikes evoked by current pulses after cGMP increased 4.8 ± 1.55 (SE) in coupled cells ($n = 19$) and 7.7 ± 2.09 (SE) in uncoupled cells ($n = 11$) ($P = 0.27$; unpaired, two-tailed *t*-test), whereas the resting membrane potential depolarized in average 4.8 ± 0.75 mV (SE) and 4.7 ± 0.87 mV (SE) in coupled ($n = 19$) and in uncoupled cells ($n = 11$), respectively ($P = 0.95$; unpaired, two-tailed *t*-test).

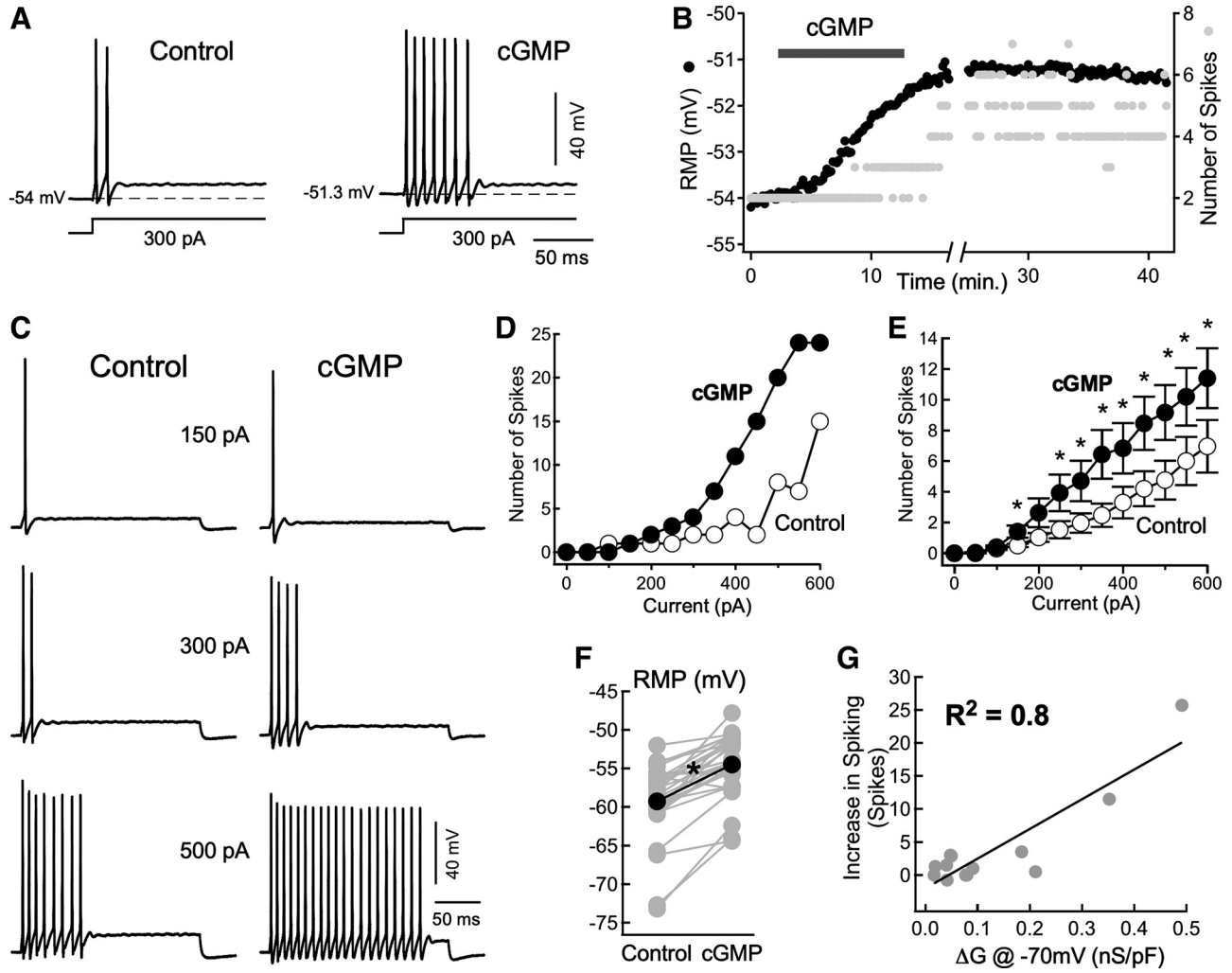

Fig. 5. cGMP modulates the firing properties and resting potential of mesencephalic trigeminal (MesV) neurons. *A*: repetitive discharge of a MesV neuron induced by a depolarizing current pulse (300 pA) in control (*left*) and after cGMP (1 mM) (*right*). *B*: plot of the resting membrane potential (RMP; left ordinates, black circles) and number of spikes (right ordinates, gray circles) of a MesV neuron evoked by depolarizing current pulses of 300 pA as a function of time before, during and after cGMP (1 mM) application to the bath. Application of cGMP is indicated by the black horizontal bar. *C*: responses of a MesV neuron to intracellular depolarizing current pulses of increasing magnitude in control (*left*) and after cGMP (*right*); 150 pA was the threshold intensity in control conditions. *D*: plot of the number of spikes evoked by current pulses of 200 ms in duration as a function of the current intensity in control (white circles) and after cGMP (black circles) for the same neuron as in *C*. *E*: plot of the mean number of spikes evoked by 200 ms current pulses as a function of the current intensity for the population of recorded cells before (white circles) and after cGMP (black circles). Error bars represent SE. *Statistically significant difference between the 2 data sets, $P < 0.05$ [$P = 0.3256$ (50 pA), $P = 0.0831$ (100 pA), $P = 0.0264$ (150 pA), $P = 0.0567$ (200 pA), $P = 0.0227$ (250 pA), $P = 0.0186$ (300 pA), $P = 0.0032$ (350 pA), $P = 0.0024$ (400 pA), $P = 0.0008$ (450 pA), $P = 0.0007$ (500 pA), $P = 0.0059$ (550 pA), $P = 0.0012$ (600 pA); paired, two-tailed *t*-test, $n = 30$ from 15 animals]. *F*: plot of the resting membrane potential values before (gray circles, control) and after cGMP (gray circles, cGMP), superimposed to the individual values are the corresponding average values in control (black circle) and after cGMP (black circle), ($P = 2.35 \times 10^{-9}$; paired, two-tailed *t*-test, $n = 30$ from 15 animals). *Significant difference, $P < 0.05$. *G*: plot of the increase in the number spikes evoked by current pulses against the increase in the hyperpolarization-activated cationic current (I_H) conductance at −70 mV after cGMP in comparison to control conditions. Data were fitted with a straight-line function and the *R*-squared value is indicated. Slope of linear regression = 45.1 ± 14.9 (95% confidence interval) represented by the continuous line; $R^2 = 0.8$, $P = 3.5 \times 10^{-5}$ ($n = 13$ from 7 animals).

Furthermore, the cGMP effects on firing were accompanied by a reduction of *Rin* of ~15%, from 108.6 ± 6.51 MΩ (SE) in control to 91.8 ± 5.83 MΩ (SE) after cGMP ($P = 1.03 \times 10^{-10}$; $n = 30$, paired, two-tailed *t*-test; Fig. 6, *A–C*), most probably as an outcome of the greater open probability of HCN channels at resting potential. Also consistent with the upregulation of the I_H, the rate of rise of pacemaker potentials during repetitive discharges showed a moderate but significant increase after cGMP (Fig. 6*D*). The slope of this potential, determined from fits to linear regressions, averaged 2.28 ± 0.18 mV/ms (SE) in control and 2.92 ± 0.27 mV/ms (SE) after cGMP ($P = 3.5 \times 10^{-5}$; $n = 18$, paired, two-tailed *t*-test; Fig. 6*E*, *left*). The acceleration of the pacemaker potential is translated in corresponding increase of the instantaneous frequency of the first interspike interval, which averaged 105.1 ± 5.84 Hz (SE) in control and 122.5 ± 7.63 Hz (SE) after cGMP ($P = 2.45 \times 10^{-6}$; $n = 18$, paired, two-tailed *t*-test; Fig. 6*E*, *right*). The increase of instantaneous frequency and of the pacemaker potential slope showed a positive correlation [slope of linear regression = 19.2 ± 6.67 (95% CI), $R^2 = 0.7$, $P = 1.5 \times 10^{-5}$; Fig. 6*F*]. Results depicted in Figs. 5 and 6 show that cGMP induces modulatory changes of MesV neuron electrophysiological properties in a highly consistent fashion, most probably through upregulation of the I_H. Supporting this no-

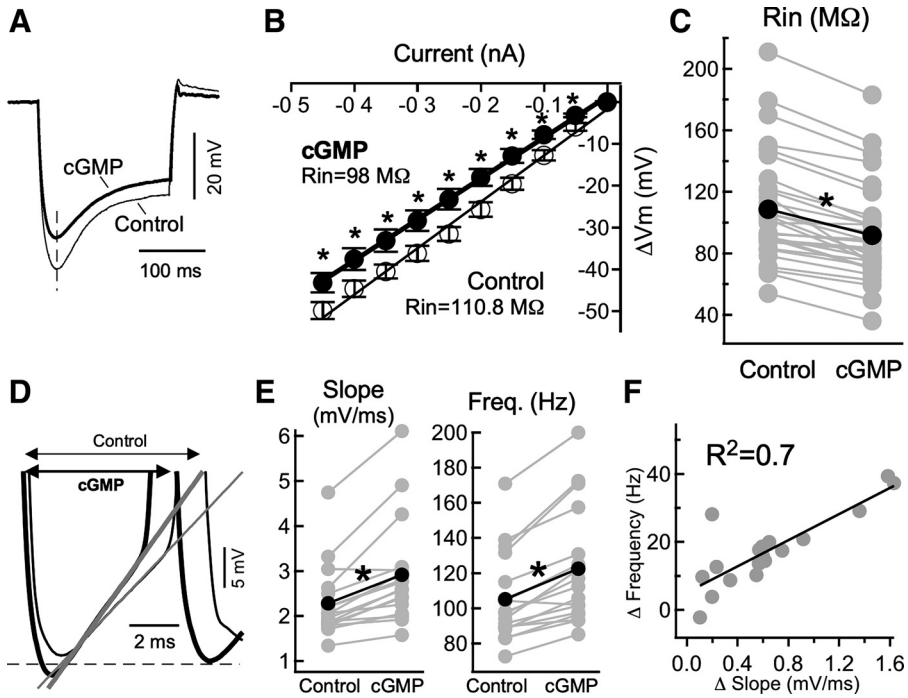

Fig. 6. cGMP effects on input resistance and subthreshold potential of mesencephalic trigeminal (MesV) neurons. *A*: voltage membrane responses of a MesV neuron to hyperpolarizing current pulses of −450 pA (control, thin trace) and after application of cGMP (thick trace). *B*: membrane voltage change versus injected current relationships obtained in the same MesV neuron as in *A* before (white circles) and after cGMP (black circles). Membrane voltage changes were measured at the time indicated by the vertical dashed line in *A*. Each value corresponds to the mean of 4 to 6 individual values, error bars indicate SD. *Statistically significant difference, $P < 0.05$ [$P = 0.3122$ (0 pA), $P = 2 \times 10^{-4}$ (−50 pA), $P = 1 \times 10^{-4}$ (−100 pA), $P = 2 \times 10^{-4}$ (−150 pA), $P = 2 \times 10^{-4}$ (−200 pA), $P = 4 \times 10^{-4}$ (−250 pA), $P = 7 \times 10^{-4}$ (−300 pA), $P = 0.0013$ (−350 pA), $P = 0.0018$ (−400 pA), $P = 0.0017$ (−450 pA); unpaired, two-tailed *t*-test] between the 2 data sets. Each curve was fitted with a straight-line function and the slope values representing the corresponding input resistance are indicated. *C*: plot of the input resistance (*Rin*) values before (gray circles, Control) and after cGMP (gray circles, cGMP) ($P = 1 \times 10^{-4}$; paired, two-tailed *t*-test). Superimposed to the values from individual cells ($n = 30$ from 15 animals) are the corresponding average values in control (black circle) and after cGMP (black circle). *Significant difference, $P < 0.05$. *D*: superimposed traces showing the membrane potential trajectory between the first 2 successive spikes of repetitive discharges evoked by depolarizing current pulses before (thin trace) and after cGMP (thick trace). Oblique straight lines indicate the slope of the pacemaker potentials for each trace. Spikes are truncated. *E*: plots showing the values of the pacemaker potential slope preceding the second spike of repetitive discharges (*left*) and instantaneous frequency (*right*) of the first interspike interval before (gray circles, Control) and after cGMP (gray circles, cGMP) (slope: $P = 3.5 \times 10^{-5}$, frequency: $P = 2.45 \times 10^{-6}$; $n = 18$ from 11 animals, paired, two-tailed *t*-test). Superimposed to the values from individual cells are the corresponding average values in control (black circle) and after cGMP (black circle). *Significant difference, $P < 0.05$. *F*: plot of the frequency increase of the first interspike interval versus the increase of the slope for the data shown in *E*. Data were fitted to a straight line. Slope of linear regression = 19.2 ± 6.67 (95% confidence interval); $R^2 = 0.7$, $P = 1.5 \times 10^{-5}$.

tion, the increase in I_H conductance at −70 mV after cGMP shows a positive correlation with the concomitant increase in firing [slope of linear regression = 45.1 ± 14.9 (95% CI), $R^2 = 0.8$, $P = 3.5 \times 10^{-5}$; Fig. 5*G*].

cGMP selectively targets the I_H of MesV neurons. While modulation of MesV neuron's firing properties by cGMP can be consistent with the upregulation of the I_H (see DISCUSSION), this does not rule out the involvement of other mechanisms as this second messenger participates in multiple signaling pathways. In fact, firing properties of neurons critically depend on the dynamic interaction between multiple voltage and ligand-gated membrane conductances that operate at both the subthreshold and the suprathreshold ranges of membrane potential. In MesV neurons, the pacemaker potential trajectory between successive spikes, critical for repetitive firing, results from the interplay between several currents (Enomoto et al. 2006; Tanaka et al. 2003; Wu et al. 2001, 2005). Among them, the I_{NaP} activates during the pacemaker potential and significantly contributes to the bursting behavior of these neurons (Enomoto et al. 2006; Wu et al. 2005). To test if cGMP actions involve the modulation of the I_{NaP}, we recorded this membrane current following standard procedures in voltage clamp by using ramp protocols (see MATERIALS AND METHODS). Noteworthy, I_{NaP} did not show any change after cGMP (1 mM), as peak current measured around −40 mV averaged −295 ± 52 pA (SE) in control and −305 ± 60 pA (SE) after cGMP ($P = 0.46$, $n = 3$; paired, two-tailed *t*-test; Fig. 7, *A*–*C*). This result excludes the possibility that the modulation of the I_{NaP} is involved in the increase of MesV neuron's excitability.

Ligand-gated channels operated by cyclic nucleotides might also significantly contribute to regulate the excitability of neurons. For instance, CNG channels are activated by cGMP and by inducing tonic depolarizations (Kaupp and Seifert 2002) can increase neuronal firing (Kawa and Sterling 2002). Noteworthy, cGMP-induced modulatory actions on excitability are accompanied by a small but highly consistent depolarization of the resting membrane potential (Fig. 5, *A*, *B*, and *F*), raising the possibility that the depolarization may be responsible for the increase in firing. To test if such a mechanism is involved in MesV neurons, we asked whether the depolarization of the membrane potential by itself is enough to explain the observed changes in firing properties induced by cGMP. First, we tried to revert the effects of cGMP on repetitive firing

by repolarizing the membrane potential to previous control levels by injecting hyperpolarizing DC current. As depicted in Fig. 7*D*, although the repolarization of the membrane potential somewhat reduces the number of spikes after cGMP, spiking is still well above control (Fig. 7*D*, compare *left* and *right*). Conversely, depolarizing the membrane potential by 4–5 mV with DC current injection in control conditions did not produce an increment in firing comparable to that induced by cGMP (Fig. 7*E*, compare *top* and *bottom*). These results are summarized in Fig. 7*F*, where the number of spikes evoked by current pulses is plotted against the membrane potential value for cells that were depolarized by DC current (squares) and for cells that were exposed to cGMP (circles). Remarkably, responses from cells exposed to cGMP present significantly more spikes than responses from cells unexposed to cGMP that were depolarized to the same level with DC current, averaging 10.5 ± 1.32 spikes (SE) and 3.8 ± 0.98 spikes (SE), respectively ($P = 6 \times 10^{-4}$, $n = 10$; unpaired, one-tailed *t*-test). Prepulse membrane potential averaged -52.4 ± 0.952 mV (SE) and -50.5 ± 1.0 (SE) in neurons exposed to cGMP and depolarized with DC current, respectively ($P = 0.179$; $n = 10$, unpaired, two-tailed *t*-test). These results show that the depolarization of the membrane potential by itself is not enough to explain the observed increase in excitability of MesV neurons, suggesting the involvement of a mechanism different than the modulation of a voltage insensitive leak-type membrane conductance.

The observed increase in neuronal firing can result not only from the acceleration of the membrane potential trajectory

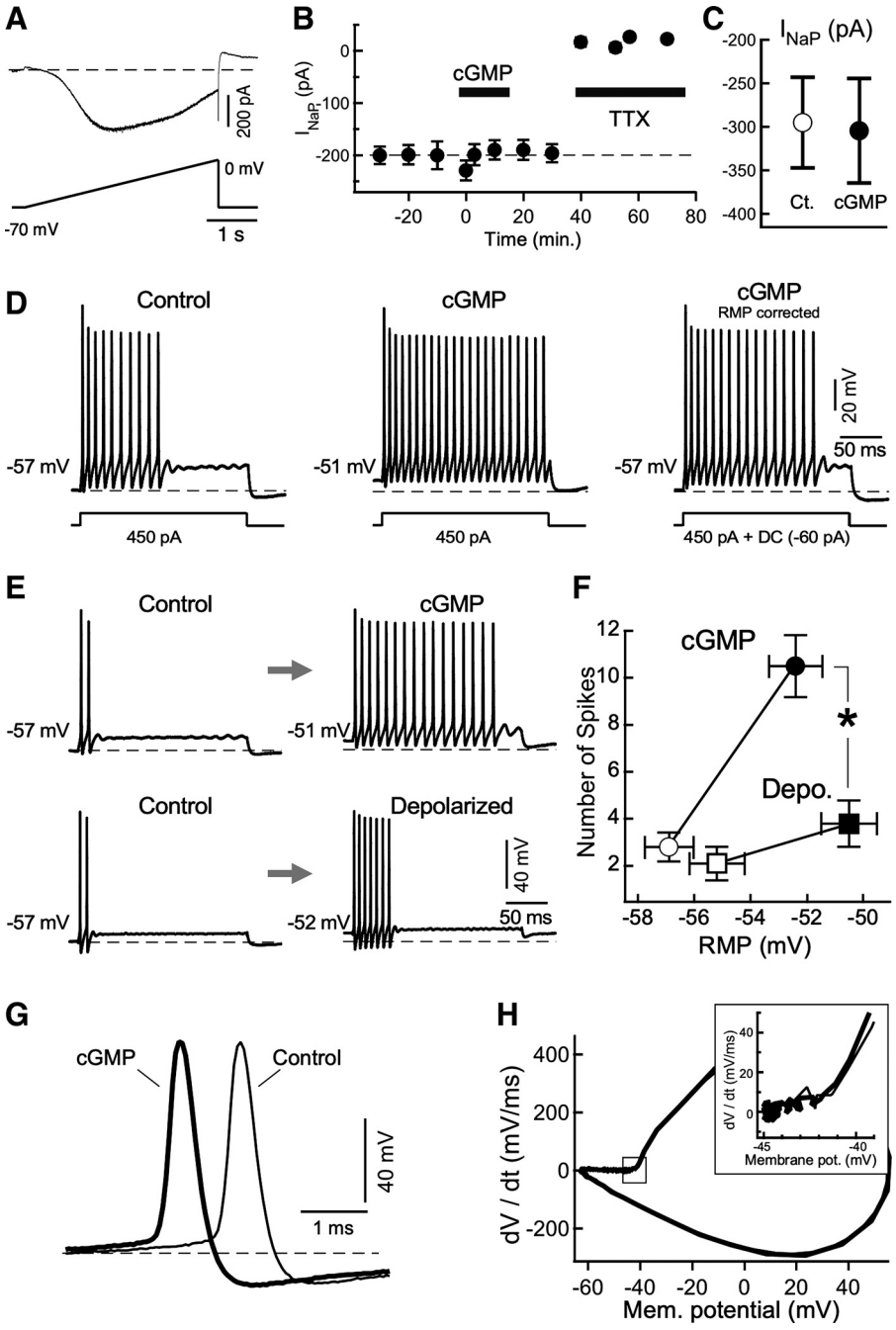

between successive spikes (pacemaker potential, Fig. 6, *D* and *E*) but also from the hyperpolarization of the voltage threshold for spike generation (lower firing level). Indeed, spike threshold was shown to be dynamically modulated with relevant consequences on neuronal excitability (Fontaine et al. 2014). To evaluate the possible contribution of such a mechanism, we examined the properties of MesV neuron's action potentials (Fig. 7*G*), particularly the spike threshold by constructing plots of the time derivative of membrane voltage versus membrane voltage (phase plots in Fig. 7*H*). The firing level determined from these plots and defined as the value of membrane voltage at which the rate of change reaches 10 mV/ms in a monotonically increasing interval did not differ significantly after cGMP (Fig. 7*H*, *inset*). This value averaged -44.0 ± 1.02 mV (SE) in control conditions and -42.4 ± 0.76 mV (SE) after cGMP ($P = 0.06$; $n = 10$, paired, two-tailed *t*-test), suggesting that cGMP did not induce changes in the spike-generating mechanisms and that the increase in excitability does not result from the lowering of the threshold for spike initiation.

The I_H is necessary for the cGMP-induced effects on neuronal excitability. The I_H can significantly contribute to the resting membrane potential, input resistance, and subthreshold behavior of neurons (Benarroch 2013; Biel et al. 2009; Robinson and Siegelbaum 2003). However, the unique biophysical properties of this conductance make difficult to unambiguously predict the functional impact of modulatory actions. Indeed, depolarization of the resting potential and acceleration of the pacemaker potential tend to increase firing, whereas the reduction of input resistance might have the opposite effect. Therefore, to obtain direct evidence indicating that the cGMP-induced changes of I_H is the mechanism responsible for the increase of MesV neuron excitability, we next asked whether this membrane conductance is necessary for the induction of such modulatory changes in excitability. For this, we studied the effects of cGMP (0.5–1 mM) in the presence of nearly saturating concentrations of the bradicardic agent ZD7288 (100 μM), which is a potent blocker of the I_H. This blocker was included in the electrode filling solution as the blocking effect of this compound is from the intracellular side of the channels (Shin et al. 2001) and at these concentrations it does not simply block the ionic current but also significantly reduces the binding of cyclic nucleotides to the channel intracellular domain (Wu et al. 2012). As expected, under these conditions MesV neuron voltage responses to hyperpolarizing current pulses lack the characteristic sag due to the activation of the I_H (Fig. 8*A*).

ZD7288 largely prevented the cGMP-induced effects on MesV neuron excitability, thus confirming our hypothesis. In fact, addition of cGMP to the bath has no effect on spiking or resting membrane potential (Fig. 8*B*). These results can be better appreciated in Fig. 8*C*, where the average resting membrane potential and number of spikes for a population of 12 cells were plotted as function of time. Confirming these results, the plot in Fig. 8*D* shows the mean number of spikes as a function of current pulse intensity before (ZD7288) and after cGMP application (cGMP + ZD7288). Spiking do not show a statistically significant increase after cGMP ($P > 0.05$, $n = 9$; paired, one-tailed *t*-test) for the whole range of tested currents. Note that although the range of current pulses explored in the presence of ZD7288 is not as extended as in control conditions, the concomitant increase in *Rin* (108.6 MΩ in control vs. 445.2 MΩ in ZD7288) suggests that the lack of effect of cGMP applications do not result from differences in stimulation protocols. Moreover, for the sample of recorded neurons ($n = 12$), the resting membrane potential do not show a statistically significant depolarization after cGMP, averaging -55.6 ± 1.38 mV (SE) before and -54.6 ± 1.13 mV (SE) after cGMP ($P = 0.135$; paired, one-tailed *t*-test; Fig. 8*E*). However, in the presence of ZD7288, cGMP applications still induce a significant reduction of the input resistance, averaging 445.2 ± 61.9 MΩ (SE) before and 381.7 ± 46.5 MΩ (SE) after cGMP ($P = 0.047$; paired, one-tailed *t*-test; Fig. 8*F*) possibly due to the modulation of a membrane mechanism different from HCN channels. These results clearly show that the I_H is necessary for the modulation of the intrinsic excitability of MesV neurons induced by cGMP, supporting the notion that the regulation of this membrane current is the underlying mechanism.

Computer simulations show that upregulation of the I_H is sufficient to induce the cGMP effects on MesV neuron excitability. The experimental results so far presented provide compelling evidence that regulation of the I_H represents the main mechanism involved in cGMP-induced increase in excitability. However, to obtain further evidence about the functional impact of such mechanism, we next asked whether the

Fig. 7. cGMP does not target other membrane conductances of mesencephalic trigeminal (MesV) neurons. *A*: representative recording of the persistent Na^+ current (I_{NaP}) in control conditions (*top trace*) in response to a voltage command consisting in a slowly rising ramp (rate ~20 mV/s) from a holding potential of -70 mV to a final potential of 0 mV (*bottom trace*). *B*: plot of the I_{NaP} magnitude (measured at the most negative value) as a function of time in another neuron in control conditions (black circles), during application of cGMP (horizontal black bar), and during application of 0.5 μM tetrodotoxin (TTX; horizontal black bar). Each value represents the average of 10 single values, and error bars represent SE *C*: summary plot of the average I_{NaP} amplitude from 3 different MesV neurons in control (white circle) and after exposure to cGMP (0.5–1 mM; black circle). Error bars represent SE ($P = 0.46$; $n = 3$ from 3 animals, paired, two-tailed *t*-test). *D*: traces showing repetitive discharges of a MesV neuron during the injection of depolarizing current pulses in control (*left*), after cGMP (*middle*), and after cGMP while the resting membrane potential was corrected to previous control levels by injecting hyperpolarizing DC current (-60 pA) (*right*). *E*, *top*: illustration of the response of a MesV neuron during injection of a depolarizing current pulse before (*left*) and after application of cGMP (*right*) showing the increase in repetitive firing and the accompanying depolarization of the resting membrane potential. *E*, *bottom*: illustration of the response to a depolarizing current pulse of another neuron that was not exposed to cGMP from resting (*left*) and from a depolarized membrane potential (*right*). During this later condition, the resting membrane potential was depolarized to a level comparable to that obtained after cGMP by injection of depolarizing DC current. In *D* and *E*, values at the *left* of each trace indicate the prepulse membrane potential and dashed horizontal lines represent the resting membrane potential level in control conditions. *F*: plot summarizing results from experiments as those shown in *E*. Average number of spikes evoked during depolarizing current pulses against the prepulse membrane potential is shown. Circles represent firing of cells before (white) and after exposure to cGMP (black). Squares represent firing of cells unexposed to cGMP at their normal resting membrane potential (white) and during depolarization with DC current injection (Depo.; black), error bars represent SE. The number of spikes evoked by current pulses is significantly larger in cells exposed to cGMP compared with cells whose resting potential was depolarized with DC current [$P = 6 \times 10^{-4}$; $n = 10$ (cells exposed to cGMP: $n = 10$ from 5 animals; depolarized cells: $n = 10$ from 3 animals), unpaired, one-tailed *t*-test]. *Significant difference, $P < 0.05$. *G*: traces showing representative action potentials before (thin trace) and after cGMP (thick trace), horizontally displaced for clarity. *H*: phase plots of the first time derivative of the membrane potential (dV/dt) against the instantaneous membrane potential, showing the rate of change of membrane potential of the traces depicted in *G*. *Inset*: larger scale of the boxed area in the phase plot.

upregulation of the I_H is enough to explain the observed changes in MesV neuron excitability after cGMP. For this, a model of a typical MesV neuron was constructed consisting in two compartments, one representing the soma and the other the axon. Six Hodgkin-Huxley type active conductances previously described in MesV neurons were inserted in our deterministic two-compartment model, whose parameters were tuned using an evolutionary multiobjective algorithm (see MATERIALS AND METHODS). Maximum densities of passive and active conductances were tuned to precisely reproduce the main electrophysiological features of MesV neurons (in control conditions) in terms of resting membrane potential, input resistance, spike amplitude and duration, and postspike afterhyperpolarization potential, as well as the main firing characteristics (see MATERIALS AND METHODS). In fact, voltage membrane responses of MesV neurons to current pulses of both polarities (Fig. 9*A*), as well as the spike waveform (Fig. 9*A*, *inset*) were faithfully reproduced by our model, indicating that the results obtained from simulations can be translated to experiments and vice versa. Thus our model represents a valuable tool to understand how the different voltage dependent membrane conductances interact to give rise to the electrophysiological phenotype of MesV neurons and the impact of I_H modulation.

Then, we investigated whether our model could reproduce the increase in excitability after upregulation of the I_H. We compared the electrophysiological properties and input-output relation of the model cell in control conditions and after modifying the I_H parameters according to our characterization of this current in voltage-clamp experiments during the effects of cGMP (I_H modulated, see MATERIALS AND METHODS). Figure 9*B* illustrates results from these simulations showing the response of the model cell in control (*top*) and after modulation of the I_H (*bottom*). Consistent with our experimental results, modulation of the I_H leads to a depolarization of the resting membrane potential, an increase in spiking and a reduction of the input resistance. The extent of these changes is also in agreement with experimental observations. The resting membrane potential of model cell changed from −58.4 mV in control to −56.0 mV after I_H modulation, whereas the number of spikes in response to current pulses of +350 pA increased from 2 spikes in control to 18 after I_H modulation (Fig. 9*B*). Additionally, upregulation of the I_H in these simulations resulted in a reduction of the input resistance of ~12% (from 113.0 to 99.6 MΩ), which is comparable to the reduction observed during experiments after addition of cGMP (~15%). Moreover, plots of the number of spikes and the frequency of the first interspike interval as a function of the intensity of current pulses show qualitatively similar results to those experimentally obtained (Fig. 5). In fact, upregulation of I_H resulted in a leftward displacement of these relations corresponding to an increase in firing, as well as a reduction of the threshold current for eliciting both single spikes and repetitive firing (Fig. 9, *C* and *D*).

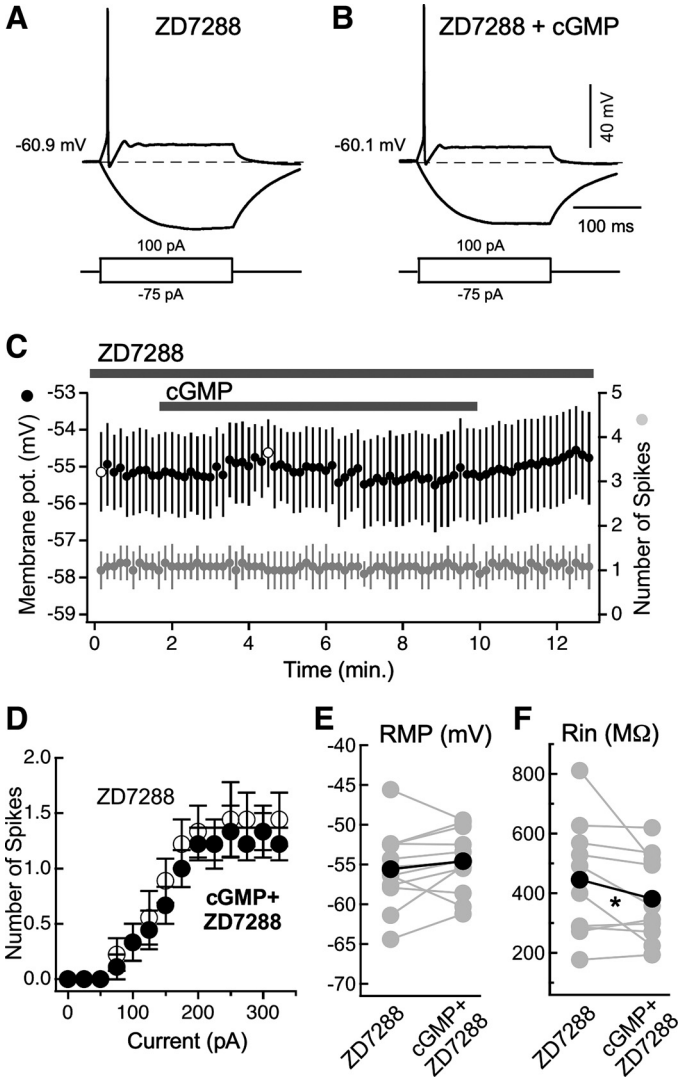

Fig. 8. The hyperpolarization-activated cationic current (I_H) is necessary for the cGMP-induced effects on neuronal excitability. *A*: sample traces of membrane voltage responses of a mesencephalic trigeminal (MesV) neuron to current pulses of 100 and −75 pA in the presence of the I_H blocker ZD7288. *B*: sample traces of membrane voltage responses of the cell shown in *A* during the same stimulation protocol after cGMP in the presence of ZD7288. *C*: plot depicts averaged values from 12 cells recorded in 5 animals of the resting membrane potential (*left* ordinates, black circles) and number of spikes evoked by depolarizing current pulses (*right* ordinates, gray circles) as a function of time before, during and after cGMP application to the bath in the presence of ZD7288. Error bars represent SE. Application of cGMP is indicated by the black horizontal bar. Peak average value of the resting membrane potential during cGMP [white circle, −54.6 ± 0.92 mV (SE)] is not statistically more depolarized in comparison to value before application [white circle, −55.1 ± 1.08 mV (SE)] $P = 0.069$; $n = 12$, paired, one-tailed *t*-test]. *D*: plot of the mean number of spikes evoked by current pulses of 200 ms in duration as a function of the current intensity for a population of recorded cells ($n = 9$ from 4 animals) in the presence of ZD7288 before (white circles) and after cGMP (black circles). Error bars represent SE. Spiking does not show a statistically significant increase after cGMP for the whole range of tested currents [*P* undefined (0 to 50 pA, identical data sets), $P = 0.83$ (75 pA), $P = 0.5$ (100 pA), $P = 0.7$ (125 pA), $P = 0.92$ (150 pA), $P = 0.78$ (175 pA), $P = 0.66$ (200 pA), $P = 0.5$ (225 pA), $P = 0.61$ (250 pA), $P = 0.83$ (275 pA), $P = 0.5$ (300 pA), $P = 0.83$ (325 pA) $n = 9$; paired, one-tailed *t*-test]. *E*: plot of the resting membrane potential values in the presence of ZD7288 before (gray circles, ZD7288) and after cGMP (gray, cGMP + ZD7288) ($P = 0.135$; $n = 12$ from 5 animals, paired, one-tailed *t*-test). *F*: plot of the input resistance values in the presence of ZD7288 before (gray circles, ZD7288) and after cGMP (gray circles, cGMP + ZD7288) ($P = 0.047$; $n = 10$ from 4 animals, paired, one-tailed *t*-test). In *E* and *F*, superimposed to the individual values are the corresponding average values in the presence of ZD7288 before (black circle) and after cGMP (black circle). *Significant difference, $P < 0.05$.

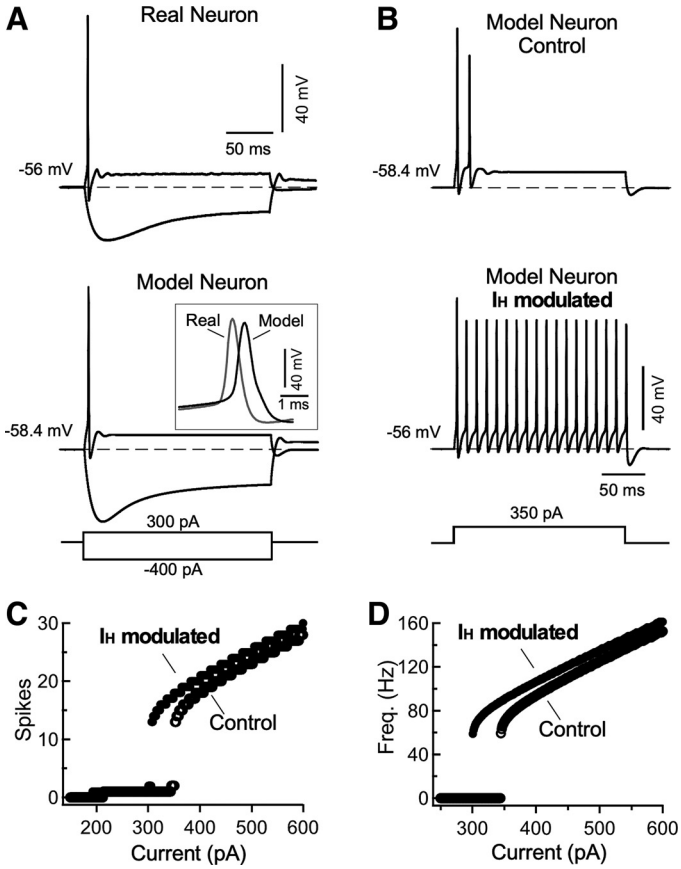

Fig. 9. Computer simulations show that upregulation of the hyperpolarization-activated cationic current (I_H) is sufficient to increase firing. *A*: comparison between real neuron and model neuron. A, *top*: a typical membrane voltage response of a mesencephalic trigeminal (MesV) neuron to depolarizing (300 pA) and hyperpolarizing (−400 pA) current pulses are illustrated. *A*, *bottom*: voltage responses of the model neuron to the same current pulses are depicted to show the similarity between real and model neuron responses. *Inset*: the spikes of the real and model neurons are displayed at an expanded temporal scale. *B*: voltage responses of the model MesV neuron to depolarizing current pulses (350 pA) in control (*top*) and after modification of the parameters defining the I_H according to the modulatory effects of the cGMP on this membrane current experimentally determined (*bottom*). Note the dramatic increase in firing and the concomitant depolarization of the resting membrane potential after changes of I_H parameters. *C*: plot of the number of spikes of the model cell evoked by current pulses of 200 ms in duration as a function of the current intensity in control (black circles, control) and after I_H modulation (black circles, I_H modulated). *D*: plot of the instantaneous frequency of the model cell of the first interspike interval during repetitive discharges evoked by depolarizing current pulses as a function of the current intensity in control (black circles, control) and after I_H modulation (black circles, I_H modulated).

These simulations show that our biophysically detailed model can reproduce the main aspects of electrophysiological properties and firing characteristics of real MesV neurons. Moreover, upregulating the I_H of model neurons has qualitatively and quantitatively similar effects on the electrophysiological properties as those experimentally observed in MesV neurons after exposure to cGMP. These findings show that upregulation of the I_H is sufficient to explain the experimentally observed increase in neuronal excitability induced by cGMP. Therefore, the upregulation of this membrane conductance by cGMP represents a valuable tool to manipulate the intrinsic excitability of MesV neurons and to study its role in coincidence detection.

cGMP enhances the gain of coincidence detection between electrically coupled MesV neurons. To test the contribution of the intrinsic excitability of neurons to coincidence detection, depolarizing current pulses of the same intensity were applied alternatively and simultaneously to coupled MesV neurons, in control conditions and after the upregulation of the I_H induced by cGMP applications (0.5–1 mM). Figure 10 shows representative results of these experiments. While bursts evoked by independent current pulses show a moderate increase after cGMP in terms of spike number (Fig. 10, *A* and *B*, compare *left* and *middle*) responses during coactivation present a dramatic increase (Fig. 10, *A* and *B*, *right*). Moreover, coincident bursts during both control and after cGMP are highly synchronic, as indicated by the cross-correlation analysis exhibiting a single peak of large magnitude and brief delay (Fig. 10, *A* and *B*, *insets*). The effect on coincidence detection gain can be better appreciated in the graph of Fig. 10*C* where the number of spikes during individual and coincident stimulation were plotted before and after the application of cGMP. In most coupled cells, the slope of this relation displays a striking increase after cGMP, indicating an increase in the gain of coincidence detection. For this population of recorded neurons ($n = 12$, from 6 pairs), the average number of spikes during independent activation showed only a modest increase from 1.81 ± 0.722 (SE) in control conditions to 3.81 ± 2.096 (SE) after cGMP ($P = 0.176$; paired, *t*-test). In contrast, the number of spikes during coactivation exhibited a much more dramatic increase from 2.9 ± 0.815 (SE) in control to 13.68 ± 3.91 (SE) after cGMP ($P = 0.0102$; paired, two-tailed *t*-test; Fig. 10*C*). Consistently, the coincidence detection index displayed a significant increase from 1.09 ± 0.19 spikes (SE) in control conditions to 9.83 ± 3.32 spikes (SE) after cGMP ($P = 0.0193$; paired, two-tailed *t*-test; Fig. 10*D*), indicating that cGMP preferentially increases firing during coactivation, thus greatly enhancing the gain of coincidence detection.

cGMP-induced enhancement of coincidence detection gain cannot be explained by changes of the strength of electrical coupling. After cGMP, presynaptic neurons are significantly more efficient in activating postsynaptic coupled neurons, consistent with its effects on coincidence detection. In fact, the spike-to-spike transfer through electrical contacts between MesV neurons is enhanced after cGMP as indicated by the ability of presynaptic trains of spikes to more faithfully recruit postsynaptic coupled cells (Fig. 11*A*). This effect was quantified by calculating the recruitment rate as the ratio of the number of postsynaptic spikes over the number of presynaptic evoked spikes. This ratio increased from 0.31 ± 0.15 (SE) in control conditions to 0.58 ± 0.16 (SE) after cGMP applications ($P = 0.0437$; $n = 10$ from 5 coupled pairs, paired, two-tailed *t*-test; Fig. 11*B*), confirming that presynaptic repetitive discharges are much more efficient in recruiting postsynaptic coupled neurons after cGMP. While this phenomenon is consistent with the modulation of the intrinsic excitability already shown, it could also result from an increase in the CC between MesV neurons. In fact, cGMP was reported to regulate the degree of coupling by targeting gap junction conductance (Hatton and Yang 1996; Rörig and Sutor 1996; Yang and Hatton 1999). To assess the possible contribution of such a mechanism, we measured the CC in control conditions and after cGMP. For this purpose, a series of hyperpolarizing current steps of different intensities were injected in one cell of

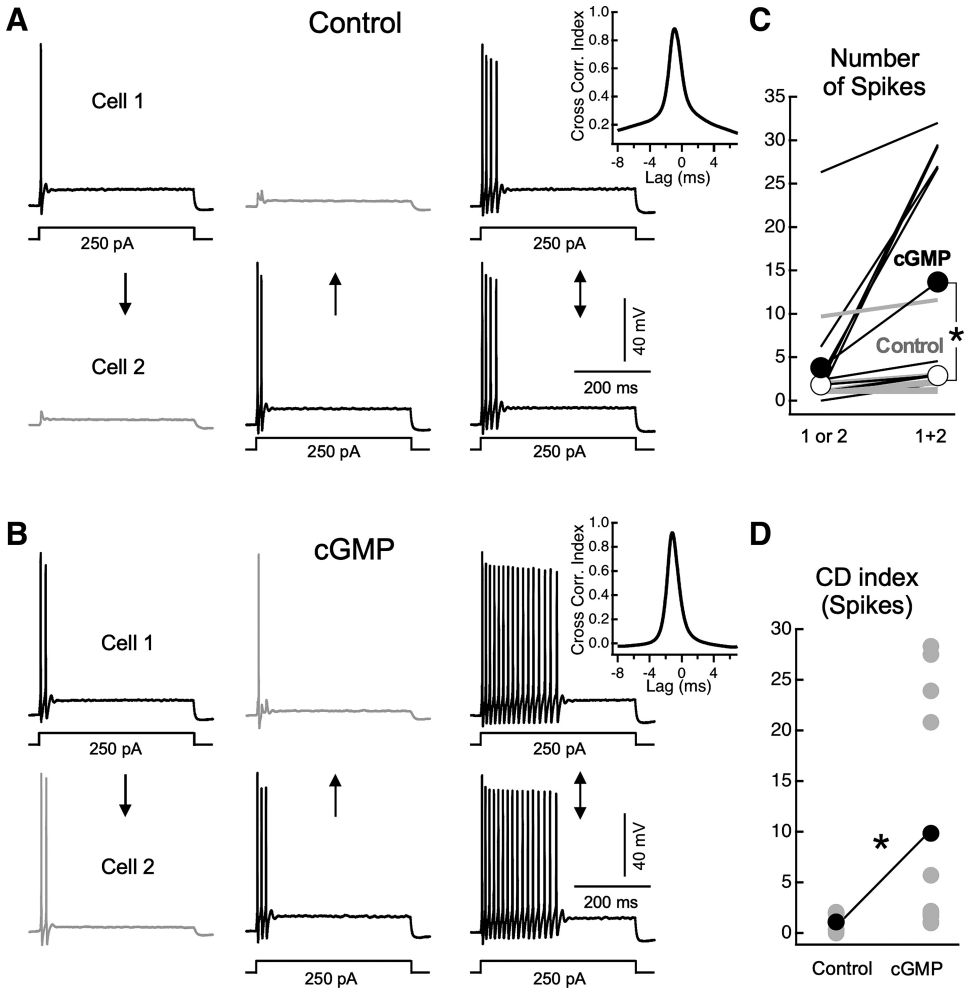

Fig. 10. cGMP enhances coincidence detection gain. *A*: membrane responses of a pair of coupled mesencephalic trigeminal (MesV) neurons during a stimulation protocol consisting in the injection of depolarizing current pulses of the same intensity (250 pA) alternatively to each cell (*left* and *middle*) and simultaneously to both cells (*right*) to show coincidence detection in control conditions. *B*: membrane responses of the same pair depicted in *A* to the same stimulation protocol after application of cGMP (1 mM) showing a dramatic increase in firing when cells were simultaneously activated indicating an increase in coincidence detection gain. *A* and *B*, *insets*: depict the cross correlograms between firing of *cells 1* and *2* during coincident activation. *C*: plot of the number of spikes when cells were independently activated (*1* or *2*) and when simultaneously activated (*1 + 2*) in control conditions (gray lines) and after cGMP (black lines). Superimposed to the values form individual neurons are the average values for the population of tested neurons in control (white circles) and after cGMP (black circles). Average values during coincident activation in each condition were statistically different ($P = 0.0096$; $n = 10$ from 6 animals, paired, two-tailed *t*-test). *D*: plot of the coincidence detection (CD) index in control conditions (gray circles) and after cGMP (gray circles) of the sample of recorded coupled cells depicted in *C*: superimposed to the values from individual neurons are the corresponding average values in control (black circle) and after cGMP (black circle) ($P = 0.019$; $n = 10$, paired, two-tailed *t*-test). *Significant difference, $P < 0.05$.

an electrically coupled pair while the induced membrane voltage changes in both cells were monitored before and after cGMP application (Fig. 11*C*). From these recordings, plots of the voltage change in the postsynaptic coupled cell as a function of the voltage change in the presynaptic injected cell were constructed and the CC was estimated from the slope of the fit to a straight line (see MATERIALS AND METHODS) (Fig. 11*D*). Instead of increasing, the CC showed a significant reduction after cGMP applications, calculated either at the beginning of voltage responses (at the peak of hyperpolarizing voltage responses) (Fig. 11*E*) or at the end (steady state, Fig. 11*F*). In fact, the CC estimated at the peak of hyperpolarizing voltage responses averaged 0.41 ± 0.05 (SE) in control conditions and 0.33 ± 0.04 (SE) after cGMP ($P = 4.46 \times 10^{-6}$; $n = 20$, paired, two-tailed *t*-test), whereas the CC estimated at steady state averaged 0.28 ± 0.03 (SE) in control and 0.23 ± 0.03 (SE) after cGMP ($P = 0.0015$; $n = 20$, paired, two-tailed). Moreover, the gap junction conductance estimated from the input and transfer resistances determined in current clamp (see MATERIALS AND METHODS) (Bennett 1966) also presented significant reduction, averaging 6.68 ± 1.08 nS (SE) in control and 6.03 ± 1.05 nS (SE) after cGMP ($P = 0.0365$; $n = 20$, paired, two-tailed; Fig. 11*H*). This suggests that the reduction of the CC, estimated from hyperpolarizing pulses, resulted from the combined reduction in *Rin* and gap junction conductance observed after cGMP application (Fig. 6, *A–C* and Fig. 11, *C–F*), as the CC depends on these two parameters (Bennett 1966; Curti and O'Brien 2016). On the other hand, coincidence detection and recruitment of postsynaptic cells depend on depolarizing rather hyperpolarizing coupling potentials. Therefore, coupling potentials evoked by presynaptic spikes (spikelets) were measured before and after cGMP application (Fig. 11*A*, *inset*). The CCs calculated from these spikelets and the presynaptic spike amplitudes (Fig. 11*G*) showed no statistical

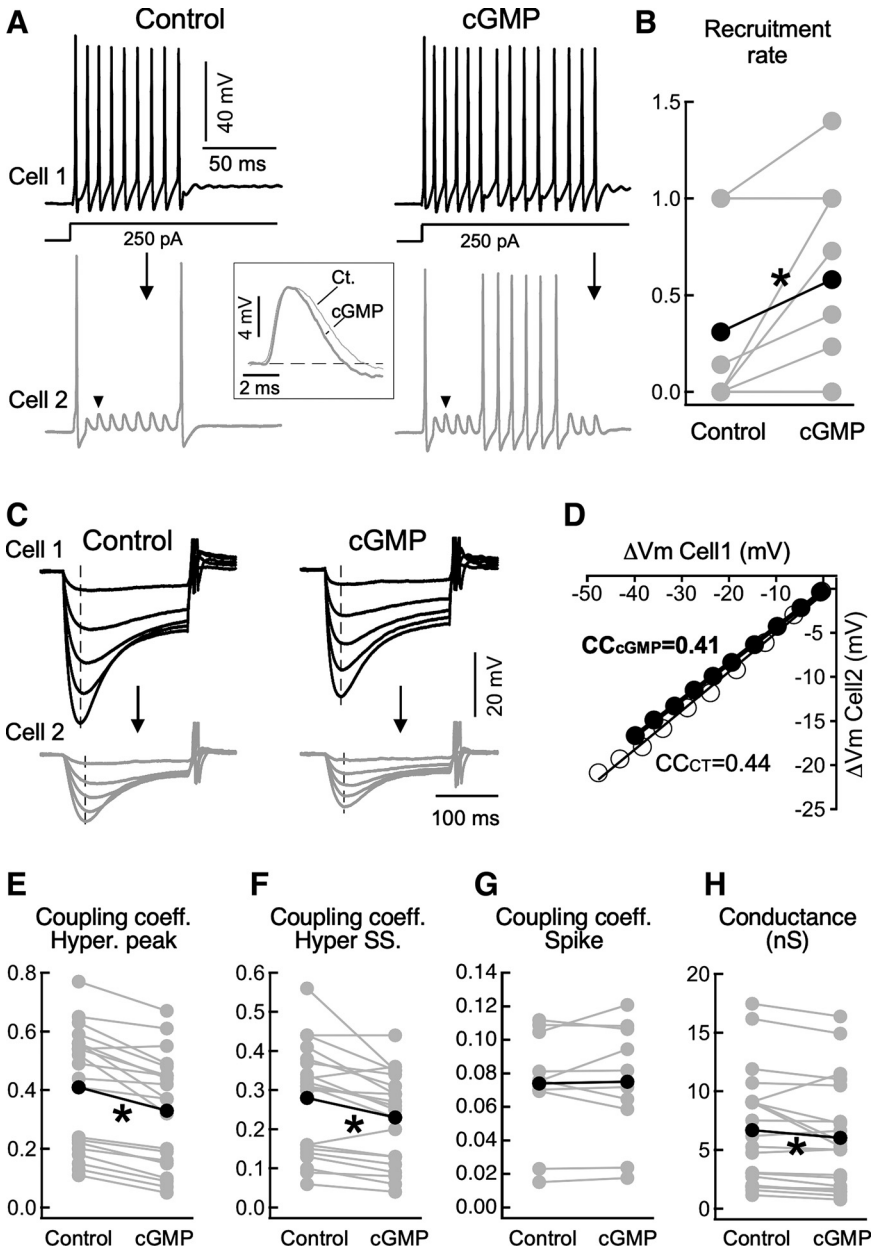

Fig. 11. cGMP-induced enhancement of coincidence detection gain does not involve changes in gap junction conductance. *A*, *left*: injection of a depolarizing current pulse (250 pA) in a cell belonging to a coupled pair evokes a repetitive discharge in this cell (*cell 1*) and corresponding coupling potentials in the postsynaptic coupled cell (*cell 2*) that eventually produce the activation of this postsynaptic neuron in control conditions. *A*, *right*: after addition of cGMP to the bath, the same stimulation protocol in the same pair of coupled mesencephalic trigeminal (MesV) neurons evokes now a more vigorous repetitive discharge in the injected cell and a marked increase in the recruitment of the postsynaptic cell. *A*, *inset*: coupling potentials (spikelets) in the postsynaptic cell indicated by downward arrowheads in corresponding traces before (control, thin trace) and after cGMP (thick trace) are displayed aligned, showing no change in amplitude. *B*: plot of recruitment rate calculated as the ratio of the number of postsynaptic spikes over the number of presynaptic evoked spikes. Individual values (gray circles) and average values for the whole sample (black circles) are illustrated superimposed ($P = 0.0437$; $n = 10$ from 5 animals, paired, two-tailed *t*-test). *C*: characterization of cGMP effects on electrical coupling in a pair of neurons. Injecting a series of hyperpolarizing current pulses of increasing intensity into one cell (*cell 1*) produces corresponding voltage responses in the injected presynaptic cell and in the postsynaptic coupled cell (*cell 2*), in control conditions (*left*), and after cGMP (*right*). *D*: from records depicted in *C* the coupling coefficient was estimated by plotting the amplitude of membrane voltage (V_m) changes (measured at the peak of hyperpolarizing responses, vertical dashed lines in *C*) in the postsynaptic cell (*cell 2*, ordinates) as a function of membrane voltage changes in the presynaptic cell (*cell 1*, abscissas) in control conditions (white circles) and after cGMP (black circles). Each data set was fitted with a straight-line function, and the slope value representing the coupling coefficients (CC) are indicated. *E*: plot of the CCs determined at the negative peak of hyperpolarizing responses before (Control) and after cGMP (cGMP) ($P = 4.46 \times 10^{-6}$; $n = 20$, paired, two-tailed *t*-test). *F*: plot of the CCs determined at steady state (SS) before (Control) and after cGMP (cGMP) ($P = 0.0015$; $n = 20$, paired, two-tailed *t*-test). *G*: plot of the coupling coefficients determined from presynaptic spikes and corresponding postsynaptic spikelets before (Control) and after cGMP (cGMP) ($P = 0.697$; $n = 10$ from 8 animals, paired, two-tailed *t*-test). *H*: plot of the gap junction conductance value before (Control) and after cGMP (cGMP) ($P = 0.0365$; $n = 20$, paired, two-tailed *t*-test). *E*, *F*, and *H* present data from the same set of neurons recorded in 9 animals. In *E*, *F*, *G*, and *H*, gray circles represent individual values in control and after cGMP exposure, respectively, and superimposed are the corresponding average values in control (black circle) and after cGMP (black circle). *Significant difference, $P < 0.05$.

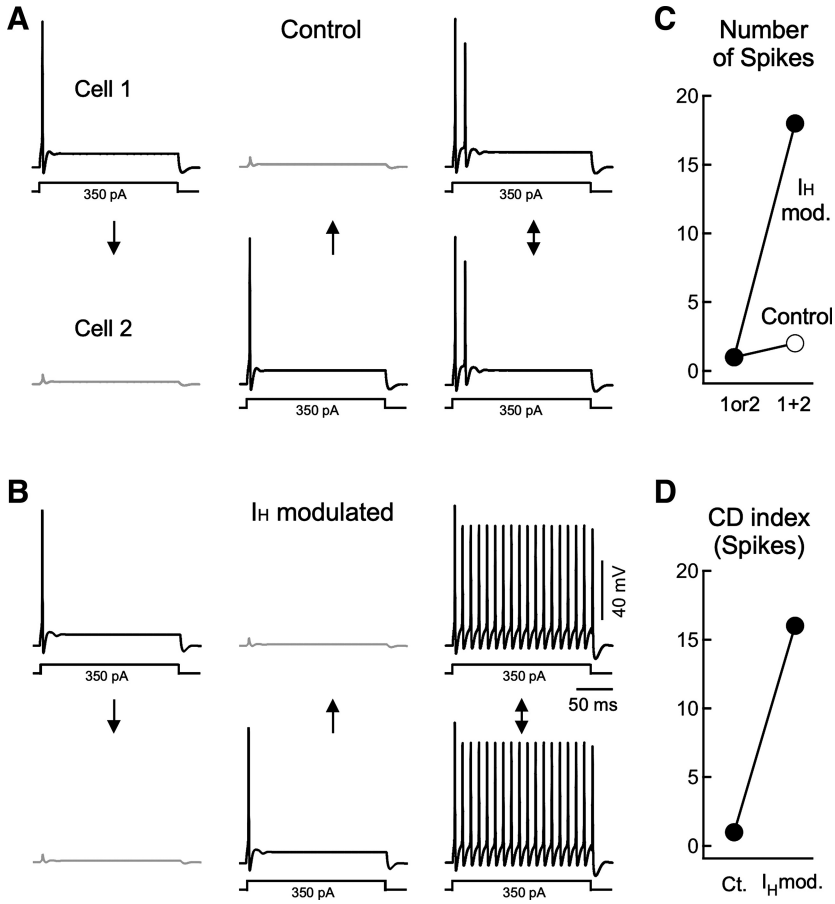

Fig. 12. Computer simulations show that upregulation of the hyperpolarization-activated cationic current (I_H) is sufficient to enhance coincidence detection gain. *A*: study of coincidence detection in a network of two coupled model mesencephalic trigeminal (MesV) neurons. Injection of depolarizing current pulses alternatively into *cells 1* or *2* induced a single action potential in the injected cell and the corresponding coupling potentials (spikelets) in the postsynaptic cell (*left* and *middle*). Simultaneous activation of these two neurons with current pulses of the same magnitude (*right*), now evoked a discharge consisting of two spikes at each cell, showing that model coupled cells support coincidence detection. *B*: after modification of the I_H parameters of both model cells according to modulatory actions of cGMP (I_H modulated), independent activation of each coupled cell with current pulses of the same intensity still evoke a single spike (*left* and *middle*). However, simultaneous activation of both neurons now induces a robust repetitive discharge (*right*). *C*: plot of the number of spikes of model cells during independently activation (*1* or *2*) and during simultaneous activation (*1 + 2*) in control conditions (white circles, control) and after modification of the I_H parameters (black circles, I_H mod.). *D*: plot of the coincidence detection (CD) index in control conditions (Ct.) and after modification of I_H parameters (I_H mod.) for the pair of model MesV neurons.

difference in control versus after cGMP as they averaged 0.074 ± 0.01 (SE) and 0.075 ± 0.011 (SE), respectively (P = 0.697; n = 10, paired, two-tailed t-test). Also, cGMP applications did not induce any significant change in the spikelet's waveform, as indicated by the values of half-amplitude duration and rise time (10–90%), which averaged 3.32 ± 0.32 ms (SE) and 0.712 ± 0.024 ms (SE), respectively, in control conditions, and 2.91 ± 0.248 ms (SE) and 0.714 ± 0.031 ms (SE), respectively, after cGMP (P = 0.076 and 0.934; n = 10, paired, two-tailed t-test). Together, this evidence shows that the enhancement in coincident detection gain do not result from changes in the strength of electrical coupling between MesV neurons. Instead, this effect most probably results from the modulation of the excitability of these neurons, highlighting the relevance of the intrinsic electrophysiological properties in determining the characteristics of coincidence detection among electrically coupled neurons.

Computer simulations show that upregulation of the I_H enhances the gain of coincidence detection in networks of electrically coupled MesV neurons. To independently evaluate if the upregulation of the I_H is enough to enhance coincidence detection gain, we extended our single cell model to a network composed of two identical coupled neurons. Because electrical coupling in the MesV nucleus is organized mostly in pairs and is supported by voltage-independent somatic gap junctions (Curti et al. 2012), electrical coupling between model cells was implemented by a simple ohmic conductance connecting the soma compartments of the two cells (see MATERIALS AND METHODS). According to experimental data, the conductance of this mechanism was set to 4 nS, which corresponded to a CC of 0.29 when measured at the peak of voltage responses to current pulses of −400 pA and of 0.22 at steady state, whereas the CC for spikes was 0.07 (not shown).

To validate these simulations, we began by investigating if this model network can support coincidence detection and then if its gain is enhanced by the upregulation of the I_H of connected cells. Coincidence detection was studied with the same stimulation protocol as during experiments; that is, suprathreshold depolarizing current pulses were injected alternatively in each cell or in both cells at the same time. As illustrated in Fig. 12*A*, injection of a +350 pA current pulse in one or the other cell induces one spike (*left* and *middle*), whereas the injection of the same current pulse in both cells at the same time induces a response consisting in two spikes in both cells (*right*), showing that this model network of coupled cells in control conditions supports coincidence detection. Remarkably, when the parameters defining the I_H were modified according to the characterization of this current after cGMP in voltage-clamp experiments (I_H modulated), the responses of model cells did not show significant changes to independent activation (Fig. 12*B*, *left* and *middle*). However, simultaneous activation of both cells induced a dramatic increase in firing compared with control condition (Fig. 12*B*, *right*). Results from these simulations are summarized in the plot of the number of spikes evoked by these stimulation protocols in control and after modulation of the I_H shown in Fig. 12*C*. These simulations show that modulation of the I_H selectively increases the susceptibility of pairs of coupled

MesV neurons to synchronic inputs, thus representing an increase in coincidence detection gain (Fig. 12*D*). These results are qualitative similar to those obtained during experiments and indicate that the excitability of coupled neurons critically determines the gain of coincidence detection.

DISCUSSION

Besides the well-known role of electrical coupling, we show here that the electrophysiological properties of coupled neurons are critical determinants of their ability to detect coincident inputs. The susceptibility or gain of this operation is highly heterogeneous across the population of MesV neurons, and experimental and theoretical evidence suggests that this heterogeneity results in part from the diverse regulatory states of the intrinsic excitability of this neuronal population. Consistently, cGMP-induced upregulation of the I_H resulted in dramatic changes in coincidence detection gain.

Coincidence detection has been extensively characterized in the auditory brainstem of birds and mammals, where fast-activating K^+ currents and morphologic dendritic specializations endow neurons with the ability to maximally respond to simultaneous inputs (Agmon-Snir et al. 1998; Joris et al. 1998; Reyes et al. 1996). Electrical synapses can also support coincidence detection (Alcamí and Pereda 2019; Connors 2017; Marder 1998). This property is based on the reduction of current leak through gap junctions during simultaneous inputs to coupled neurons (cancellation of the loading effect), resulting in larger membrane voltage changes that facilitate neuronal activation (Di Garbo et al. 2006; Hjorth et al. 2009; Rela and Szczupak 2004). Thus a defining characteristic of coincidence detection is that simultaneous depolarizing inputs evoke stronger neuronal firing in comparison to independent inputs, as shown in Fig. 1, *A–D*. However, there is no a clear limit to establish, based solely on its time dependency or precision, if a given neuron or neural circuit operates as a coincidence detector or not. Precision, whether in the microsecond or in the millisecond range is most probably related to the specific function of the neural network (Alonso et al. 1996; Carr and Konishi 1990; König et al. 1996; Roy and Alloway 2001; Usrey et al. 2000). Regardless of the underlying mechanism, coincidence detection is an emergent property involved in brain functions like sound source localization (Carr 1993; Joris et al. 1998), information processing (König et al. 1996), organization of motor outputs (Edwards et al. 1998), sensorimotor integration (Rabinowitch et al. 2013), improvement of signal-to-noise ratio (DeVries et al. 2002; Smith and Vardi 1995), and Hebbian learning (Tsien 2000).

Coincidence detection in the MesV nucleus is heterogeneous and is critically determined by the intrinsic excitability of neurons. While both precision (time window over which inputs are summated) and gain (contrast between maximal and minimal responses) are critical aspects of coincidence detection, precision and its determinants have been previously characterized in different structures, including the auditory system (Agmon-Snir et al. 1998; Reyes et al. 1996) and populations of electrically coupled neurons (Alcami 2018; Edwards et al. 1998; Vervaeke et al. 2010). In contrast, much less is known about the determinants of the gain of coincidence detection. Therefore, we focused our efforts in characterizing this particular aspect and its underlying mechanisms by using stimulation protocols expected to cause maximal contrast between responses, that is, coincident versus independent depolarizing inputs. The spatial segregation of synaptic inputs to electrotonically coupled cellular compartments is among the mechanisms that maximize this contrast, like in neurons of the auditory brainstem that present bipolar dendrites and synaptic inputs that are segregated to each dendrite. In these neurons, coincidence detection is based on the nonlinear summation of excitatory inputs and the function of each dendrite as a current sink for inputs to the other dendrite (Agmon-Snir et al. 1998). Pairs of coupled MesV neurons seem to operate in a similar fashion, wherein each neuron of a coupled pair acts as a current sink for the other, pointing toward the coupling strength as the primary determinant of the gain of coincidence detection.

Nevertheless, heterogeneity in coincidence detection gain across the population of MesV neurons cannot be explained solely in terms of the diversity of coupling strengths. Indeed, while high susceptibility to coincident inputs was displayed almost exclusively by strongly coupled pairs, the reciprocal is not true. This indicates that strong coupling is a necessary condition, although not sufficient, for high gain coincidence detection. On the other hand, highly excitable neurons tend to be more susceptible to coincident inputs unlike low excitable ones. This strongly suggests that neuronal excitability plays, along with electrical coupling, a key role determining the susceptibility of coupled neurons to coincident inputs. Consistent with a prominent role of the neuronal intrinsic properties, cGMP-induced increase in neuronal excitability resulted in a dramatic enhancement of coincidence detection gain. Such changes in coincidence detection were not accompanied by a concomitant increase of spike-triggered coupling potentials, emphasizing the role of the intrinsic excitability. Thus electrical coupling, in conjunction with the active electrophysiological properties, endows circuits of coupled neurons with an efficient mechanism to selectively respond to simultaneous or coincident inputs, as opposed to asynchronous or randomly distributed ones, that is, to act as coincidence detectors.

cGMP-induced upregulation of the I_H increases MesV neuron's excitability and coincidence detection gain. We show that the I_H is sharply modulated by cGMP as reported previously (Datunashvili et al. 2018; Ingram and Williams 1996; Wilson and Garthwaite 2010; Yang and Hatton 1999). This modulation results in an enhancement of MesV neuron excitability, as was shown in cardiac (Brown et al. 1979) and other neural cells (Bobker and Williams 1989; Cardenas et al. 1999; Maccaferri and McBain 1996; McCormick and Pape 1990a; Tang and Trussell 2015). This is most probably due to an increase of the net inward current at membrane voltage values close to the resting potential. Two lines of evidence support this conclusion. First, in the presence of the I_H blocker ZD7288, cGMP is unable to modulate MesV neuron spiking and resting potential. Second, computer simulations show that changes in I_H parameters, consistent with experimental observations, faithfully reproduce the actions of cGMP. Together, these findings indicate that I_H modulation is necessary and sufficient to mediate the cGMP-induced increase in excitability. However, I_H has also been reported to reduce excitability rather than to boost it (Berger et al. 2003; Magee 1998; Stuart and Spruston 1998; Tsay et al. 2007; Williams and Stuart 2000), and upregulation of this conductance results in a de-

crease of neuronal output (Fan et al. 2005; Poolos et al. 2002; Rosenkranz and Johnston 2006). This contradictory role of I_H on neuronal excitability is most likely due to the unique biophysical properties of this conductance. In fact, I_H is activated by hyperpolarization and presents a reversal potential around −30 mV, resulting in an inward current that promotes firing by bringing membrane voltage closer to its firing level. On the other hand, activation of this conductance results in a reduction of the neuron's input resistance dampening the impact of excitatory inputs (Dyhrfjeld-Johnsen et al. 2009; Lippert and Booth 2009; Migliore and Migliore 2012). Which of these outcomes on excitability prevail seems to be related to the spatial distribution of HCN channels in relation to the spiking compartment, most typically the cell body (Harnett et al. 2015). In fact, when located at, or close to the soma compartment, upregulation of the I_H results in an increase of neuronal excitability (Cardenas et al. 1999; Kanyshkova et al. 2009; McCormick and Pape 1990b; Pál et al. 2003; Tang and Trussell 2015; Tu et al. 2004), whereas at distal locations of the dendritic compartment its activation tends to reduce excitability (Fan et al. 2005; Lörincz et al. 2002; Notomi and Shigemoto 2004; Poolos et al. 2002; Rosenkranz and Johnston 2006; Wang et al. 2007). Moreover, this conductance seems to be tonically active, supporting an inward current at membrane potentials between the spike afterhyperpolarization potential and its reversion, even in the time course of the interspike interval, whose duration is several orders of magnitude shorter than the I_H activation time constant.

The upregulation of the I_H preferentially increases firing of coupled MesV neurons during simultaneous depolarizations. In fact, spiking during coincident depolarizing inputs showed a dramatic increase after cGMP, whereas spiking during independent depolarizations displayed little change. This most probably results from the contrasting actions of I_H on cellular excitability in combination with the loading effect displayed by pairs of coupled neurons. In control conditions, the loading effect reduces on average the *Rin* of coupled cells by ~26%, supporting the reduced neuronal spiking during asynchronous inputs in comparison to coincident inputs, thus allowing coupled neurons to act as coincidence detectors. After I_H upregulation, coupled neurons show an additional reduction of their *Rin* of between 10% and 15%. This results from the same cell's *Rin* reduction plus the reduction of the *Rin* of the coupled cell. This additional reduction in *Rin* is not translated into a corresponding reduction in firing, most probably thanks to the concomitant increase in net inward current. Thus during uncorrelated inputs to coupled neurons, the reduction of the *Rin* and the increase in inward current seem to compensate each other. However, under the I_H modulated condition, by canceling the loading effect, coincident inputs mitigate part of the *Rin* reduction, potentiating the action of the increased inward current on membrane excitability, and supporting strong repetitive discharges. Therefore, the upregulation of the I_H increases the contrast between minimal and maximal neuronal responses evoked during uncorrelated and coincident inputs, respectively, thus enhancing the susceptibility of pairs of coupled MesV neurons to coincident inputs. This conclusion is supported by our computer simulations that show a marked increase in firing of model cells during simultaneous depolarizations under I_H modulated conditions.

Functional relevance. MesV neurons are primary afferents that innervate muscle spindles of jaw-closing muscles or mechanoreceptors of periodontal ligaments and establish direct excitatory contacts with trigeminal motoneurons (Morquette et al. 2012). These afferents are strongly activated during jaw movements associated to food intake, thus providing positive proprioceptive feedback for the adjustment of bite force (Lavigne et al. 1987; Yamamoto et al. 1989). Based on our results, it is possible that coincident activation promotes stronger firing of coupled MesV neurons, operating as an amplification mechanism for this sensory input, facilitating jaw-closing muscle activation. Also, the somas of MesV neurons receive synaptic inputs from several brain areas, suggesting that they participate in the organization of orofacial behaviors by integrating sensory information from the periphery with inputs from hierarchically superior structures (Kolta et al. 1990; Nagy et al. 1986). Inputs from the supratrigeminal area evoke short latency excitatory postsynaptic potentials strong enough to induce or enhance oscillatory activity that eventually leads to firing (Verdier et al. 2004). Our findings show that coincident depolarizing inputs to coupled cells promote strong repetitive firing, suggesting that pairs of coupled MesV neurons that share same excitatory inputs will tend to produce synchronic bursts. These synchronic bursts most likely represent strong excitatory inputs onto trigeminal motoneurons. In fact, beyond supporting temporal summation of excitatory postsynaptic potentials, bursts are considered to be robust codes of communication at chemical junctions since they facilitate transmitter release from low probability contacts (Lisman 1997). Moreover, individual I_a afferents typically evoke weak synaptic actions (Mendell and Henneman 1971), implying that summation of coincident inputs from multiple afferents is required to activate motoneurons. Remarkably, we found that the cGMP-induced modulation of the I_H greatly enhances the gain of coincidence detection, increasing the duration of repetitive discharges, most probably reinforcing excitatory inputs onto trigeminal motoneurons. Because MesV neurons massively project to trigeminal motoneurons (Stanek et al. 2014), this suggests that such modulatory actions significantly impact on the organization of orofacial behaviors. In addition, MesV neurons receive nitrergic projections and nitric oxide increases the excitability of these neurons most probably through elevations of intracellular cGMP levels (Pose et al. 2003). Histaminergic projections to the MesV nucleus were also described (Inagaki et al. 1987), and histamine actions have also been shown to involve cGMP in other systems (Hatton and Yang 1996; Hough 1999). This suggests that modulation of coincidence detection between coupled MesV neurons may occur under physiological conditions.

Recent evidence shows that pairs of electrically interconnected GABAergic interneurons from the cortex and the cerebellum are coinnervated, supporting synchronous depolarizing inputs to these interneurons (Otsuka and Kawaguchi 2013; van Welie et al. 2016). This suggests that coincidence detection represents a common feature of networks of coupled neurons of the mammalian brain. In the retina of mammals, electrical coupling between cones and between AII amacrine cells underlies a noise reduction operation through a mechanism analogous to coincidence detection (DeVries et al. 2002; Smith and Vardi 1995), where simultaneous (signal specific) inputs have a larger impact on

membrane potential in comparison to randomly distributed (noisy) ones (Sterling and Demb 2004). It is tempting to speculate that by modulating coincidence detection gain as shown here, the output of these circuits can be readily altered with relevant functional consequences. In fact, HCN channels and electrical synapses have been shown to coexist in many neuronal populations, raising the possibility that circuit operations supported by electrical coupling like coincidence detection are under precise and dynamic regulatory control through modulation of the highly modifiable I_H current.

ACKNOWLEDGMENTS

We thank Alberto Pereda and Inés Pose for critical discussions and comments on an early version of this manuscript.

GRANTS

This work was supported by Agencia Nacional de Investigación e Innovación, Uruguay (FCE_1_2014_1_104725) and Comisión Académica de Posgrado of Universidad de la República.

DISCLOSURES

No conflicts of interest, financial or otherwise, are declared by the authors.

AUTHOR CONTRIBUTIONS

F.D. and S.C. conceived and designed research; F.D. and S.C. performed experiments; F.D. and S.C. analyzed data; F.D. and S.C. interpreted results of experiments; F.D. and S.C. edited and revised manuscript; F.D. and S.C. approved final version of manuscript; S.C. prepared figures; S.C. drafted manuscript.

REFERENCES

Agmon-Snir H, Carr CE, Rinzel J. The role of dendrites in auditory coincidence detection. *Nature* 393: 268–272, 1998. doi:10.1038/30505.

Alcami P. Electrical synapses enhance and accelerate interneuron recruitment in response to coincident and sequential excitation. *Front Cell Neurosci* 12: 156, 2018. doi:10.3389/fncel.2018.00156.

Alcamí P, Pereda AE. Beyond plasticity: the dynamic impact of electrical synapses on neural circuits. *Nat Rev Neurosci* 20: 253–271, 2019. doi:10.1038/s41583-019-0133-5.

Alonso J-M, Usrey WM, Reid RC. Precisely correlated firing in cells of the lateral geniculate nucleus. *Nature* 383: 815–819, 1996. doi:10.1038/383815a0.

Angelo K, Margrie TW. Population diversity and function of hyperpolarization-activated current in olfactory bulb mitral cells. *Sci Rep* 1: 50, 2011. doi:10.1038/srep00050.

Bahl A, Stemmler MB, Herz AV, Roth A. Automated optimization of a reduced layer 5 pyramidal cell model based on experimental data. *J Neurosci Methods* 210: 22–34, 2012. doi:10.1016/j.jneumeth.2012.04.006.

Benarroch EE. HCN channels: function and clinical implications. *Neurology* 80: 304–310, 2013. doi:10.1212/WNL.0b013e31827dec42.

Bennett MV. Physiology of electrotonic junctions. *Ann N Y Acad Sci* 137: 509–539, 1966. doi:10.1111/j.1749-6632.1966.tb50178.x.

Bennett MV, Zukin RS. Electrical coupling and neuronal synchronization in the Mammalian brain. *Neuron* 41: 495–511, 2004. doi:10.1016/S0896-6273(04)00043-1.

Berger T, Senn W, Lüscher HR. Hyperpolarization-activated current I_h disconnects somatic and dendritic spike initiation zones in layer V pyramidal neurons. *J Neurophysiol* 90: 2428–2437, 2003. doi:10.1152/jn.00377.2003.

Biel M, Wahl-Schott C, Michalakis S, Zong X. Hyperpolarization-activated cation channels: from genes to function. *Physiol Rev* 89: 847–885, 2009. doi:10.1152/physrev.00029.2008.

Bobker DH, Williams JT. Serotonin augments the cationic current Ih in central neurons. *Neuron* 2: 1535–1540, 1989. doi:10.1016/0896-6273(89)90041-X.

Brown H, Difrancesco D, Noble S. Cardiac pacemaker oscillation and its modulation by autonomic transmitters. *J Exp Biol* 81: 175–204, 1979..

Canavos G. *Applied Probability and Statistical Methods*. New York: Little, Brown, 1988.

Cardenas CG, Mar LP, Vysokanov AV, Arnold PB, Cardenas LM, Surmeier DJ, Scroggs RS. Serotonergic modulation of hyperpolarization-activated current in acutely isolated rat dorsal root ganglion neurons. *J Physiol* 518: 507–523, 1999. doi:10.1111/j.1469-7793.1999.0507p.x.

Carr CE. Processing of temporal information in the brain. *Annu Rev Neurosci* 16: 223–243, 1993. doi:10.1146/annurev.ne.16.030193.001255.

Carr CE, Konishi M. A circuit for detection of interaural time differences in the brain stem of the barn owl. *J Neurosci* 10: 3227–3246, 1990. doi:10.1523/JNEUROSCI.10-10-03227.1990.

Chillemi B, Barbi M, Di Garbo A. A network of interneurons coupled by electrical synapses behaves as a coincidence detector. In: *International Work-Conference on the Interplay Between Natural and Artificial Computation*, edited by Mira J, Álvarez JR, editors. Berlin, Germany: Springer, 2007, p. 81–89.

Connors BW. Synchrony and so much more: Diverse roles for electrical synapses in neural circuits. *Dev Neurobiol* 77: 610–624, 2017. doi:10.1002/dneu.22493.

Connors BW, Long MA. Electrical synapses in the mammalian brain. *Annu Rev Neurosci* 27: 393–418, 2004. doi:10.1146/annurev.neuro.26.041002.131128.

Curti S, Hoge G, Nagy JI, Pereda AE. Synergy between electrical coupling and membrane properties promotes strong synchronization of neurons of the mesencephalic trigeminal nucleus. *J Neurosci* 32: 4341–4359, 2012. doi:10.1523/JNEUROSCI.6216-11.2012.

Curti S, O'Brien J. Characteristics and plasticity of electrical synaptic transmission. *BMC Cell Biol* 17, *Suppl* 1: 13, 2016. doi:10.1186/s12860-016-0091-y.

Datunashvili M, Chaudhary R, Zobeiri M, Lüttjohann A, Mergia E, Baumann A, Balfanz S, Budde B, van Luijtelaar G, Pape HC, Koesling D, Budde T. Modulation of hyperpolarization-activated inward current and thalamic activity modes by different cyclic nucleotides. *Front Cell Neurosci* 12: 369, 2018. doi:10.3389/fncel.2018.00369.

Del Negro CA, Chandler SH. Physiological and theoretical analysis of K^+ currents controlling discharge in neonatal rat mesencephalic trigeminal neurons. *J Neurophysiol* 77: 537–553, 1997. doi:10.1152/jn.1997.77.2.537.

Devor A, Yarom Y. Electrotonic coupling in the inferior olivary nucleus revealed by simultaneous double patch recordings. *J Neurophysiol* 87: 3048–3058, 2002. doi:10.1152/jn.2002.87.6.3048.

DeVries SH, Qi X, Smith R, Makous W, Sterling P. Electrical coupling between mammalian cones. *Curr Biol* 12: 1900–1907, 2002. doi:10.1016/S0960-9822(02)01261-7.

Di Garbo A, Barbi M, Chillemi S. Signal processing properties of fast spiking interneurons. *Biosystems* 86: 27–37, 2006. doi:10.1016/j.biosystems.2006.03.009.

Dugué GP, Brunel N, Hakim V, Schwartz E, Chat M, Lévesque M, Courtemanche R, Léna C, Dieudonné S. Electrical coupling mediates tunable low-frequency oscillations and resonance in the cerebellar Golgi cell network. *Neuron* 61: 126–139, 2009. doi:10.1016/j.neuron.2008.11.028.

Dyhrfjeld-Johnsen J, Morgan RJ, Soltesz I. Double trouble? Potential for hyperexcitability following both channelopathic up- and downregulation of I(h) in epilepsy. *Front Neurosci* 3: 25–33, 2009. doi:10.3389/neuro.01.005.2009.

Edwards DH, Yeh SR, Krasne FB. Neuronal coincidence detection by voltage-sensitive electrical synapses. *Proc Natl Acad Sci USA* 95: 7145–7150, 1998. doi:10.1073/pnas.95.12.7145.

Enomoto A, Han JM, Hsiao CF, Chandler SH. Sodium currents in mesencephalic trigeminal neurons from $Na_v1.6$ null mice. *J Neurophysiol* 98: 710–719, 2007. doi:10.1152/jn.00292.2007.

Enomoto A, Han JM, Hsiao CF, Wu N, Chandler SH. Participation of sodium currents in burst generation and control of membrane excitability in mesencephalic trigeminal neurons. *J Neurosci* 26: 3412–3422, 2006. doi:10.1523/JNEUROSCI.5274-05.2006.

Fan Y, Fricker D, Brager DH, Chen X, Lu HC, Chitwood RA, Johnston D. Activity-dependent decrease of excitability in rat hippocampal neurons through increases in I(h). *Nat Neurosci* 8: 1542–1551, 2005. doi:10.1038/nn1568.

Fleidervish IA, Gutnick MJ. Kinetics of slow inactivation of persistent sodium current in layer V neurons of mouse neocortical slices. *J Neurophysiol* 76: 2125–2130, 1996. doi:10.1152/jn.1996.76.3.2125.

Fontaine B, MacLeod KM, Lubejko ST, Steinberg LJ, Köppl C, Peña JL. Emergence of band-pass filtering through adaptive spiking in the owl's cochlear nucleus. *J Neurophysiol* 112: 430–445, 2014. doi:10.1152/jn.00132.2014.

Forti L, Cesana E, Mapelli J, D'Angelo E. Ionic mechanisms of autorhythmic firing in rat cerebellar Golgi cells. *J Physiol* 574: 711–729, 2006. doi:10.1113/jphysiol.2006.110858.

Galarreta M, Hestrin S. Spike transmission and synchrony detection in networks of GABAergic interneurons. *Science* 292: 2295–2299, 2001. doi:10.1126/science.1061395.

Getting PA. Modification of neuron properties by electrotonic synapses. I. Input resistance, time constant, and integration. *J Neurophysiol* 37: 846–857, 1974. doi:10.1152/jn.1974.37.5.846.

Harnett MT, Magee JC, Williams SR. Distribution and function of HCN channels in the apical dendritic tuft of neocortical pyramidal neurons. *J Neurosci* 35: 1024–1037, 2015. doi:10.1523/JNEUROSCI.2813-14.2015.

Hatton GI, Yang QZ. Synaptically released histamine increases dye coupling among vasopressinergic neurons of the supraoptic nucleus: mediation by H1 receptors and cyclic nucleotides. *J Neurosci* 16: 123–129, 1996. doi:10.1523/JNEUROSCI.16-01-00123.1996.

Hines ML, Davison AP, Muller E. NEURON and Python. *Front Neuroinform* 3: 1, 2009. doi:10.3389/neuro.11.001.2009.

Hjorth J, Blackwell KT, Kotaleski JH. Gap junctions between striatal fast-spiking interneurons regulate spiking activity and synchronization as a function of cortical activity. *J Neurosci* 29: 5276–5286, 2009. doi:10.1523/JNEUROSCI.6031-08.2009.

Hough LB. Histamine. In: *Basic Neurochemistry*, edited by Siegel GJ. Philadelphia, PA: Lippincott-Raven, 1999, p. 293–313.

Inagaki N, Yamatodani A, Shinoda K, Shiotani Y, Tohyama M, Watanabe T, Wada H. The histaminergic innervation of the mesencephalic nucleus of the trigeminal nerve in rat brain: a light and electron microscopical study. *Brain Res* 418: 388–391, 1987. doi:10.1016/0006-8993(87)90109-0.

Ingram SL, Williams JT. Modulation of the hyperpolarization-activated current (Ih) by cyclic nucleotides in guinea-pig primary afferent neurons. *J Physiol* 492: 97–106, 1996. doi:10.1113/jphysiol.1996.sp021292.

Johnston J, Forsythe ID, Kopp-Scheinpflug C. Going native: voltage-gated potassium channels controlling neuronal excitability. *J Physiol* 588: 3187–3200, 2010. doi:10.1113/jphysiol.2010.191973.

Joris PX, Smith PH, Yin TC. Coincidence detection in the auditory system: 50 years after Jeffress. *Neuron* 21: 1235–1238, 1998. doi:10.1016/S0896-6273(00)80643-1.

Kang Y, Notomi T, Saito M, Zhang W, Shigemoto R. Bidirectional interactions between h-channels and Na^+-K^+ pumps in mesencephalic trigeminal neurons. *J Neurosci* 24: 3694–3702, 2004. doi:10.1523/JNEUROSCI.5641-03.2004.

Kanyshkova T, Pawlowski M, Meuth P, Dubé C, Bender RA, Brewster AL, Baumann A, Baram TZ, Pape HC, Budde T. Postnatal expression pattern of HCN channel isoforms in thalamic neurons: relationship to maturation of thalamocortical oscillations. *J Neurosci* 29: 8847–8857, 2009. doi:10.1523/JNEUROSCI.0689-09.2009.

Kaupp UB, Seifert R. Cyclic nucleotide-gated ion channels. *Physiol Rev* 82: 769–824, 2002. doi:10.1152/physrev.00008.2002.

Kawa F, Sterling P. cGMP modulates spike responses of retinal ganglion cells via a cGMP-gated current. *Vis Neurosci* 19: 373–380, 2002. doi:10.1017/S0952523802193138.

Khakh BS, Henderson G. Hyperpolarization-activated cationic currents (Ih) in neurones of the trigeminal mesencephalic nucleus of the rat. *J Physiol* 510: 695–704, 1998. doi:10.1111/j.1469-7793.1998.00695.x.

Kolta A, Lund JP, Rossignol S. Modulation of activity of spindle afferents recorded in trigeminal mesencephalic nucleus of rabbit during fictive mastication. *J Neurophysiol* 64: 1067–1076, 1990. doi:10.1152/jn.1990.64.4.1067.

König P, Engel AK, Singer W. Integrator or coincidence detector? The role of the cortical neuron revisited. *Trends Neurosci* 19: 130–137, 1996. doi:10.1016/S0166-2236(96)80019-1.

Landisman CE, Long MA, Beierlein M, Deans MR, Paul DL, Connors BW. Electrical synapses in the thalamic reticular nucleus. *J Neurosci* 22: 1002–1009, 2002. doi:10.1523/JNEUROSCI.22-03-01002.2002.

Lavigne G, Kim JS, Valiquette C, Lund JP. Evidence that periodontal pressoreceptors provide positive feedback to jaw closing muscles during mastication. *J Neurophysiol* 58: 342–358, 1987. doi:10.1152/jn.1987.58.2.342.

Lazarov NE. Comparative analysis of the chemical neuroanatomy of the mammalian trigeminal ganglion and mesencephalic trigeminal nucleus. *Prog Neurobiol* 66: 19–59, 2002. doi:10.1016/S0301-0082(01)00021-1.

Liem RS, Copray JC, van Willigen JD. Ultrastructure of the rat mesencephalic trigeminal nucleus. *Acta Anat (Basel)* 140: 112–119, 1991. doi:10.1159/000147045.

Lippert A, Booth V. Understanding effects on excitability of simulated I (h) modulation in simple neuronal models. *Biol Cybern* 101: 297–306, 2009. doi:10.1007/s00422-009-0337-2.

Lisman JE. Bursts as a unit of neural information: making unreliable synapses reliable. *Trends Neurosci* 20: 38–43, 1997. doi:10.1016/S0166-2236(96)10070-9.

Lörincz A, Notomi T, Tamás G, Shigemoto R, Nusser Z. Polarized and compartment-dependent distribution of HCN1 in pyramidal cell dendrites. *Nat Neurosci* 5: 1185–1193, 2002. doi:10.1038/nn962.

Lüthi A, McCormick DA. H-current: properties of a neuronal and network pacemaker. *Neuron* 21: 9–12, 1998. doi:10.1016/S0896-6273(00)80509-7.

Maccaferri G, Mangoni M, Lazzari A, DiFrancesco D. Properties of the hyperpolarization-activated current in rat hippocampal CA1 pyramidal cells. *J Neurophysiol* 69: 2129–2136, 1993. doi:10.1152/jn.1993.69.6.2129.

Maccaferri G, McBain CJ. The hyperpolarization-activated current (Ih) and its contribution to pacemaker activity in rat CA1 hippocampal stratum oriens-alveus interneurones. *J Physiol* 497: 119–130, 1996. doi:10.1113/jphysiol.1996.sp021754.

Magee JC. Dendritic hyperpolarization-activated currents modify the integrative properties of hippocampal CA1 pyramidal neurons. *J Neurosci* 18: 7613–7624, 1998. doi:10.1523/JNEUROSCI.18-19-07613.1998.

Marder E. Electrical synapses: beyond speed and synchrony to computation. *Curr Biol* 8: R795–R797, 1998. doi:10.1016/S0960-9822(07)00502-7.

McCormick DA, Pape HC. Noradrenergic and serotonergic modulation of a hyperpolarization-activated cation current in thalamic relay neurones. *J Physiol* 431: 319–342, 1990a. doi:10.1113/jphysiol.1990.sp018332.

McCormick DA, Pape HC. Properties of a hyperpolarization-activated cation current and its role in rhythmic oscillation in thalamic relay neurones. *J Physiol* 431: 291–318, 1990b. doi:10.1113/jphysiol.1990.sp018331.

Mendell LM, Henneman E. Terminals of single Ia fibers: location, density, and distribution within a pool of 300 homonymous motoneurons. *J Neurophysiol* 34: 171–187, 1971. doi:10.1152/jn.1971.34.1.171.

Mercer A, Bannister AP, Thomson AM. Electrical coupling between pyramidal cells in adult cortical regions. *Brain Cell Biol* 35: 13–27, 2006. doi:10.1007/s11068-006-9005-9.

Migliore M, Migliore R. Know your current I(h): interaction with a shunting current explains the puzzling effects of its pharmacological or pathological modulations. *PLoS One* 7: e36867, 2012. doi:10.1371/journal.pone.0036867.

Morquette P, Lavoie R, Fhima MD, Lamoureux X, Verdier D, Kolta A. Generation of the masticatory central pattern and its modulation by sensory feedback. *Prog Neurobiol* 96: 340–355, 2012. doi:10.1016/j.pneurobio.2012.01.011.

Müller F, Scholten A, Ivanova E, Haverkamp S, Kremmer E, Kaupp UB. HCN channels are expressed differentially in retinal bipolar cells and concentrated at synaptic terminals. *Eur J Neurosci* 17: 2084–2096, 2003. doi:10.1046/j.1460-9568.2003.02634.x.

Nagy JI, Buss M, Daddona PE. On the innervation of trigeminal mesencephalic primary afferent neurons by adenosine deaminase-containing projections from the hypothalamus in the rat. *Neuroscience* 17: 141–156, 1986. doi:10.1016/0306-4522(86)90232-0.

Notomi T, Shigemoto R. Immunohistochemical localization of Ih channel subunits, HCN1-4, in the rat brain. *J Comp Neurol* 471: 241–276, 2004. doi:10.1002/cne.11039.

Otsuka T, Kawaguchi Y. Common excitatory synaptic inputs to electrically connected cortical fast-spiking cell networks. *J Neurophysiol* 110: 795–806, 2013. doi:10.1152/jn.00071.2013.

Pál B, Pór A, Szucs G, Kovács I, Rusznák Z. HCN channels contribute to the intrinsic activity of cochlear pyramidal cells. *Cell Mol Life Sci* 60: 2189–2199, 2003. doi:10.1007/s00018-003-3187-4.

Pape HC. Queer current and pacemaker: the hyperpolarization-activated cation current in neurons. *Annu Rev Physiol* 58: 299–327, 1996. doi:10.1146/annurev.ph.58.030196.001503.

Pedroarena CM, Pose IE, Yamuy J, Chase MH, Morales FR. Oscillatory membrane potential activity in the soma of a primary afferent neuron. *J Neurophysiol* 82: 1465–1476, 1999. doi:10.1152/jn.1999.82.3.1465.

Perez Velazquez JL, Carlen PL. Gap junctions, synchrony and seizures. *Trends Neurosci* 23: 68–74, 2000. doi:10.1016/S0166-2236(99)01497-6.

Poolos NP, Migliore M, Johnston D. Pharmacological upregulation of h-channels reduces the excitability of pyramidal neuron dendrites. *Nat Neurosci* 5: 767–774, 2002. doi:10.1038/nn891.

Pose I, Sampogna S, Chase MH, Morales FR. Mesencephalic trigeminal neurons are innervated by nitric oxide synthase-containing fibers and respond to nitric oxide. *Brain Res* 960: 81–89, 2003. doi:10.1016/S0006-8993(02)03776-9.

Publio R, Oliveira RF, Roque AC. A computational study on the role of gap junctions and rod Ih conductance in the enhancement of the dynamic range of the retina. *PLoS One* 4: e6970, 2009. doi:10.1371/journal.pone.0006970.

Rabinowitch I, Chatzigeorgiou M, Schafer WR. A gap junction circuit enhances processing of coincident mechanosensory inputs. *Curr Biol* 23: 963–967, 2013. doi:10.1016/j.cub.2013.04.030.

Rateau Y, Ropert N. Expression of a functional hyperpolarization-activated current (I_h) in the mouse nucleus reticularis thalami. *J Neurophysiol* 95: 3073–3085, 2006. doi:10.1152/jn.00922.2005.

Rela L, Szczupak L. Gap junctions: their importance for the dynamics of neural circuits. *Mol Neurobiol* 30: 341–357, 2004. doi:10.1385/MN:30:3:341.

Reyes AD, Rubel EW, Spain WJ. In vitro analysis of optimal stimuli for phase-locking and time-delayed modulation of firing in avian nucleus laminaris neurons. *J Neurosci* 16: 993–1007, 1996. doi:10.1523/JNEUROSCI.16-03-00993.1996.

Robinson RB, Siegelbaum SA. Hyperpolarization-activated cation currents: from molecules to physiological function. *Annu Rev Physiol* 65: 453–480, 2003. doi:10.1146/annurev.physiol.65.092101.142734.

Rörig B, Sutor B. Nitric oxide-stimulated increase in intracellular cGMP modulates gap junction coupling in rat neocortex. *Neuroreport* 7: 569–572, 1996. doi:10.1097/00001756-199601310-00046.

Rosenkranz JA, Johnston D. Dopaminergic regulation of neuronal excitability through modulation of Ih in layer V entorhinal cortex. *J Neurosci* 26: 3229–3244, 2006. doi:10.1523/JNEUROSCI.4333-05.2006.

Roy SA, Alloway KD. Coincidence detection or temporal integration? What the neurons in somatosensory cortex are doing. *J Neurosci* 21: 2462–2473, 2001. doi:10.1523/JNEUROSCI.21-07-02462.2001.

Saito M, Murai Y, Sato H, Bae YC, Akaike T, Takada M, Kang Y. Two opposing roles of 4-AP-sensitive K^+ current in initiation and invasion of spikes in rat mesencephalic trigeminal neurons. *J Neurophysiol* 96: 1887–1901, 2006. doi:10.1152/jn.00176.2006.

Schoppa NE, Westbrook GL. AMPA autoreceptors drive correlated spiking in olfactory bulb glomeruli. *Nat Neurosci* 5: 1194–1202, 2002. doi:10.1038/nn953.

Schweighofer N, Doya K, Kawato M. Electrophysiological properties of inferior olive neurons: A compartmental model. *J Neurophysiol* 82: 804–817, 1999. doi:10.1152/jn.1999.82.2.804.

Shin KS, Rothberg BS, Yellen G. Blocker state dependence and trapping in hyperpolarization-activated cation channels: evidence for an intracellular activation gate. *J Gen Physiol* 117: 91–101, 2001. doi:10.1085/jgp.117.2.91.

Smith RG, Vardi N. Simulation of the AII amacrine cell of mammalian retina: functional consequences of electrical coupling and regenerative membrane properties. *Vis Neurosci* 12: 851–860, 1995. doi:10.1017/S095252380000941X.

Stanek E IV, Cheng S, Takatoh J, Han BX, Wang F. Monosynaptic premotor circuit tracing reveals neural substrates for oro-motor coordination. *eLife* 3: e02511, 2014. doi:10.7554/eLife.02511.

Sterling P, Demb JB. Retina, in *The Synaptic Organization of the Brain*, edited by Shepherd GM. New York: Oxford Univerity Press, 2004, p. 217–269.

Sterratt DC. Q10: the effect of temperature on ion channel kinetics. In: *Encyclopedia of Computational Neuroscience*, edited by Jaeger D, Jung R. New York: Springer, 2014, p. 2551–2552.

Stuart G, Spruston N. Determinants of voltage attenuation in neocortical pyramidal neuron dendrites. *J Neurosci* 18: 3501–3510, 1998. doi:10.1523/JNEUROSCI.18-10-03501.1998.

Tanaka S, Chandler SH. Serotonergic modulation of persistent sodium currents and membrane excitability via cyclic AMP-protein kinase A cascade in mesencephalic V neurons. *J Neurosci Res* 83: 1362–1372, 2006. doi:10.1002/jnr.20822.

Tanaka S, Wu N, Hsaio CF, Turman J Jr, Chandler SH. Development of inward rectification and control of membrane excitability in mesencephalic v neurons. *J Neurophysiol* 89: 1288–1298, 2003. doi:10.1152/jn.00850.2002.

Tang ZQ, Trussell LO. Serotonergic regulation of excitability of principal cells of the dorsal cochlear nucleus. *J Neurosci* 35: 4540–4551, 2015. doi:10.1523/JNEUROSCI.4825-14.2015.

Trenholm S, McLaughlin AJ, Schwab DJ, Awatramani GB. Dynamic tuning of electrical and chemical synaptic transmission in a network of motion coding retinal neurons. *J Neurosci* 33: 14927–14938, 2013. doi:10.1523/JNEUROSCI.0808-13.2013.

Tsay D, Dudman JT, Siegelbaum SA. HCN1 channels constrain synaptically evoked Ca2+ spikes in distal dendrites of CA1 pyramidal neurons. *Neuron* 56: 1076–1089, 2007. doi:10.1016/j.neuron.2007.11.015.

Tsien JZ. Linking Hebb's coincidence-detection to memory formation. *Curr Opin Neurobiol* 10: 266–273, 2000. doi:10.1016/S0959-4388(00)00070-2.

Tu H, Deng L, Sun Q, Yao L, Han J-S, Wan Y. Hyperpolarization-activated, cyclic nucleotide-gated cation channels: roles in the differential electrophysiological properties of rat primary afferent neurons. *J Neurosci Res* 76: 713–722, 2004. doi:10.1002/jnr.20109.

Usrey WM, Alonso JM, Reid RC. Synaptic interactions between thalamic inputs to simple cells in cat visual cortex. *J Neurosci* 20: 5461–5467, 2000. doi:10.1523/JNEUROSCI.20-14-05461.2000.

van Welie I, Roth A, Ho SSN, Komai S, Häusser M. Conditional spike transmission mediated by electrical coupling ensures millisecond precision-correlated activity among interneurons in vivo. *Neuron* 90: 810–823, 2016. doi:10.1016/j.neuron.2016.04.013.

Verdier D, Lund JP, Kolta A. Synaptic inputs to trigeminal primary afferent neurons cause firing and modulate intrinsic oscillatory activity. *J Neurophysiol* 92: 2444–2455, 2004. doi:10.1152/jn.00279.2004.

Veruki ML, Hartveit E. AII (Rod) amacrine cells form a network of electrically coupled interneurons in the mammalian retina. *Neuron* 33: 935–946, 2002a. doi:10.1016/S0896-6273(02)00609-8.

Veruki ML, Hartveit E. Electrical synapses mediate signal transmission in the rod pathway of the mammalian retina. *J Neurosci* 22: 10558–10566, 2002b. doi:10.1523/JNEUROSCI.22-24-10558.2002.

Vervaeke K, Lőrincz A, Gleeson P, Farinella M, Nusser Z, Silver RA. Rapid desynchronization of an electrically coupled interneuron network with sparse excitatory synaptic input. *Neuron* 67: 435–451, 2010. doi:10.1016/j.neuron.2010.06.028.

Wang LY, Gan L, Forsythe ID, Kaczmarek LK. Contribution of the Kv3.1 potassium channel to high-frequency firing in mouse auditory neurones. *J Physiol* 509: 183–194, 1998. doi:10.1111/j.1469-7793.1998.183bo.x.

Wang M, Ramos BP, Paspalas CD, Shu Y, Simen A, Duque A, Vijayraghavan S, Brennan A, Dudley A, Nou E, Mazer JA, McCormick DA, Arnsten AF. α2A-adrenoceptors strengthen working memory networks by inhibiting cAMP-HCN channel signaling in prefrontal cortex. *Cell* 129: 397–410, 2007. doi:10.1016/j.cell.2007.03.015.

Wang Y, Barakat A, Zhou H. Electrotonic coupling between pyramidal neurons in the neocortex. *PLoS One* 5: e10253, 2010. doi:10.1371/journal.pone.0010253.

Williams SR, Stuart GJ. Site independence of EPSP time course is mediated by dendritic I_h in neocortical pyramidal neurons. *J Neurophysiol* 83: 3177–3182, 2000. doi:10.1152/jn.2000.83.5.3177.

Wilson GW, Garthwaite J. Hyperpolarization-activated ion channels as targets for nitric oxide signalling in deep cerebellar nuclei. *Eur J Neurosci* 31: 1935–1945, 2010. doi:10.1111/j.1460-9568.2010.07226.x.

Wu N, Enomoto A, Tanaka S, Hsiao CF, Nykamp DQ, Izhikevich E, Chandler SH. Persistent sodium currents in mesencephalic v neurons participate in burst generation and control of membrane excitability. *J Neurophysiol* 93: 2710–2722, 2005. doi:10.1152/jn.00636.2004.

Wu N, Hsiao CF, Chandler SH. Membrane resonance and subthreshold membrane oscillations in mesencephalic V neurons: participants in burst generation. *J Neurosci* 21: 3729–3739, 2001. doi:10.1523/JNEUROSCI.21-11-03729.2001.

Wu S, Gao W, Xie C, Xu X, Vorvis C, Marni F, Hackett AR, Liu Q, Zhou L. Inner activation gate in S6 contributes to the state-dependent binding of cAMP in full-length HCN2 channel. *J Gen Physiol* 140: 29–39, 2012. doi:10.1085/jgp.201110749.

Yamamoto T, Matsuo R, Kiyomitsu Y, Kitamura R. Sensory and motor responses of trigeminal and reticular neurons during ingestive behavior in rats. *Exp Brain Res* 76: 386–400, 1989. doi:10.1007/BF00247896.

Yang J, Xing JL, Wu NP, Liu YH, Zhang CZ, Kuang F, Han VZ, Hu SJ. Membrane current-based mechanisms for excitability transitions in neurons of the rat mesencephalic trigeminal nuclei. *Neuroscience* 163: 799–810, 2009. doi:10.1016/j.neuroscience.2009.07.007.

Yang QZ, Hatton GI. Nitric oxide via cGMP-dependent mechanisms increases dye coupling and excitability of rat supraoptic nucleus neurons. *J Neurosci* 19: 4270–4279, 1999. doi:10.1523/JNEUROSCI.19-11-04270.1999.